

POLITECNICO DI TORINO
Master Degree in Biomedical Engineering



**A computational hemodynamic
exploration of novel
arterio-venous graft designs**

Supervisor

Prof. Umberto Morbiducci

Co-Supervisors

Ing. Diego Gallo

Ing. Giuseppe De Nisco

Candidate

Katia Siciliano

06 April 2018

E quindi uscimmo a riveder le stelle.

Dante Alighieri

A mia madre e mio padre

Abstract

About 2 million patients worldwide per year are affected by end stage renal disease (ESRD) with a reduction of kidneys functionality below 10% with respect to healthy conditions. Treatments of ESRD are kidney transplantation or renal replacement therapies, such as hemodialysis. A successful hemodialysis procedure needs a permanent vascular access. In most patients, the first choice is an arterio-venous fistula, however, in elderly or diabetics, because of the lower vessels quality, an arterio-venous graft (AVG) represents the second best option. Hereby, unlike the arterio-venous fistula, the connection between an artery and a vein is provided by a synthetic graft. However, AVGs implanting is very limited, if compared to other type of vascular access, due to deriving complications. AV grafts are at risk of thrombosis and stenosis formation, making them unusable and leading to thrombectomy interventions or to explant. Stenosis, and consequently thrombosis, results from neointimal hyperplasia which mainly occurs at venous anastomosis and in the draining vein. These adverse events, are driven by abnormal hemodynamics. AVG insertion, indeed, causes an alteration of physiological hemodynamics, with the insorgence of low wall shear stress (WSS), high oscillatory shear stress and high residence time areas at luminal surface. These condition of "disturbed shear" lead to vessel remodelling and neointimal hyperplasia.

In this contest, enhancing long-term patency of AVG is an ongoing challenge of clinicians and bioengineers. For this purpose, many studies have been conducted and several AVG geometries have been proposed. More in detail, several studies have been conducted in order to investigate the capacity of different AVG geometries to replicate and promote the physiological helical flow, which tends to

reduce unfavorable hemodynamic conditions (e.g. flow separation areas).

In this scenario, the aim of this study is to investigate the efficiency of novel arterio-venous graft design, avoiding neointimal hyperplasia onset. In detail, six novel AVG models have been created, presenting a flow divider splitting blood flow in three parts. In three of these AVG models, the flow divider rotates around the central axis forming three helical shaped channels (HFD models); the other three have been obtained by fixing the position of the flow divider along the graft (LFD models). Three flow divider position have been tested. In order to evaluate the possible benefits of these novel designs, two more models have been reconstructed basing on commercially available AVGs: one replicating the straight conventional structure, and one other imitating the helical conformation of the SwirlGraft (Veryan Medical).

The finite volume method was used to solve Navier-Stokes equations. More in detail, the eight models were meshed by using the solid meshing commercial software Ansys ICEM®. Fluid motion, under unsteady-state conditions, was simulated by using the software Ansys Fluent®. Blood was considered as a Newtonian fluid with constant density and dynamic viscosity, equal to 1060 kg/m^3 and 3.5 cP respectively. Measured flow rate was prescribed as inflow boundary condition. The 95% of the inflow was sent to the graft (with a further downstream division of 90% to the proximal vein and 5% to the distal vein), and 5% to distal artery. No-slip conditions was imposed at the luminal surface.

Simulations results were analyzed in terms of both near-wall and bulkflow hemodynamic descriptors. Concerning near-wall hemodynamics, the "well-established" WSS-based descriptors, i.e., TAWSS, OSI and RRT, were computed. The analysis was focused on a region of interest (ROI) at the venous anastomosis. As proposed in previous study, objective thresholds for "disturbed shear" were defined, pooling data from the eight simulations and identifying the lower (upper) 20th percentile value for TAWSS (for OSI and RRT) at the venous anastomosis. ROI surface area exposed to OSI and RRT above, or TAWSS below, their respective threshold values was calculated. Bulk flow hemodynamics was evaluated in terms of helicity-based descriptors and recirculation volume.

Simulation results show that the insertion of a flow divider in AVGs influences

the downstream hemodynamics modifying the percentage of vein surface area exposed to "disturbed shear". More in detail, LFD configurations exhibit worse performances with respect to the other simulated models, determining lower mean values of TAWSS, and higher mean values of OSI and RRT at the venous anastomosis. On the contrary, the helical geometry of HFD grafts can be instrumental in suppressing disturbed shear in the venous segment. HFD models, indeed, lead to higher values of TAWSS at the ROI with respect to the straight model. However, ROI surface area exposed to unfavorable hemodynamic conditions depends on helix pitch and flow divider positioning.

Among HFD models, HFD-3 results to be the best in suppressing adverse hemodynamic conditions. Comparing obtained results for HFD-3 model with respect to the other simulated AVG models, it can be clearly observed that: HFD-3 model (1) exhibits an athero-protective behaviour at the venous anastomosis, with the increase (decrease) of TAWSS (OSI and RRT) mean values, and (2) guarantees the lowest amount of recirculation volume in the draining vein, organizing blood fluid structures in only one big vortex toward the heart.

Contents

1	Introduction	1
1.1	Cardiovascular system	2
1.1.1	Blood vessels	2
1.1.2	Arteries	3
1.1.3	Veins	5
1.1.4	Blood	5
1.2	Kidney failure	7
1.2.1	Acute kidney injury (AKI)	7
1.2.2	Chronic kidney disease (CKD)	8
1.3	Hemodialysis	9
1.4	Vascular accesses	10
1.4.1	Arterio-venous graft	12
1.4.2	Complications of vascular accesses	13
1.5	Intimal Hyperplasia: the cause of vascular access failure	15
1.5.1	Hemodynamics and intimal hyperplasia	16
1.6	A literature review	17
1.6.1	Bulk flow	17
1.6.2	Researches enhancing AVG patency	18
1.7	Research goal	21
2	Materials and methods	22
2.1	Arterio-venous graft (AVG) models	23
2.2	Computational mesh	26
2.2.1	Computational setting for mesh sensitivity	27

2.2.2	Mesh sensitivity analysis	27
2.3	Unsteady-state simulations	32
2.3.1	Governing equations	32
2.3.2	Computational setting and boundary conditions	33
2.4	Methods for analysis	34
2.4.1	Wall Shear Stress	34
2.4.2	WSS - based descriptors	35
2.4.3	Region of interest	36
2.4.4	Helicity	37
2.4.5	Helicity - based descriptors	38
2.4.6	Recirculating flow volume	40
3	Results and discussion	41
3.1	Velocity	42
3.2	WSS-based descriptors	48
3.2.1	WSS-based descriptors in region of interest	54
3.3	Helicity-based descriptors	64
3.4	Recirculating flow volume	68
4	Conclusions	71
	Bibliography	75
A		79
A.1	Selection of ROI	79
B		81
B.1	Axial velocity	81
B.2	Recirculating flow volume	82

List of Figures

1.1	The circulatory system: oxygenated blood flow in arteries while deoxygenated blood returns to the heart through the veins.	2
1.2	Representation of blood vessels: large elastic arteries leave the heart and branch to form muscular arteries. These arteries branch further and enter organs, where they branch much further to form arterioles and then capillaries. Blood returns back to the heart through venous system, which increases its diameter by moving from capillaries to large vein.	4
1.3	Hemodialysis circuit	10
1.4	Types of vascular access: venous catheter, autogenous fistula and arteriovenous graft.	11
1.5	Four different anastomotic configurations: A) Side-to-side anastomosis, B) End-to-end anastomosis, C) End-to-side anastomosis, and D) Side-to-end anastomosis	12
1.6	Prosthetic graft configurations in the upper and lower extremities: a) curved brachio-axillary, b) looped axillo-axillary, c) forearm straight brachio-basilic, d) looped radial to cubital fossa vein, e) looped saphenous vein-femoral artery, f) straight saphenous vein-femoral artery. . .	13
1.7	Vessels remodelling and onset of Intimal hyperplasia	17
1.8	Arterio-venous grafts commercially available. a) Straight conventional graft, b) Spiral Flow graft 1, c) Cuffed arterio-venous graft [2], d) Swirl graft (Veryan Medical).	20

2.1	Base arterio-venous graft model anastomosed to an artery and a vein. Vessels are divided in a proximal zone, in which flow normally, while in distal section a small flow rate is sent.	23
2.2	AVG models: AVGs Base and Helical doesn't have flow divider, while AVGs LFD and HFD have flow divider witch differs for its position (1-2-3) and its helical pitch (HFD).	24
2.3	Cross-section of flow divider	25
2.4	Grid with tetrahedral elements in the core region and prismatic elements in the boundary layer. a. Boundary layer thick 0.5 mm and 10 layers.; b. Boundary layer thick 0.3 mm and 5 layers; c. Boundary layer thick 0.5 mm and 10 layers, cross section of flow divider.	28
2.5	Percentage differences of mean WSS of all grids with respect to that of Mesh 11.	30
2.6	Percentage differences of mean WSS of only grids with 10 layers and thickness boundary layer of 0.5mm with respect to that of Mesh 11.	30
2.7	Percentual differences of maximum WSS of only grids with 10 layers and thickness boundary layer of 0.5mm with respect to those Mesh 11	31
2.8	Flow waveform of post-operative vascular access patient.	34
2.9	Velocity distribution of blood in a vessel	35
2.10	Representation of ROI in AVG model.	37
2.11	Helicity representation [28].	38
3.1	Velocity magnitude contours and in-plane streamlines at early systole (0.090 s) for two different cross section: at venous anastomosis (section A) and 10 mm downstream of that (section B).	43
3.2	Velocity magnitude contours and in-plane streamlines at peak systole (0.185 s).	44
3.3	Velocity magnitude contours and in-plane streamlines at late systole (0.340 s).	45
3.4	Velocity vectors at a cross-section of flow divider.	46
3.5	Time-averaged velocity contour levels of a cross-section along x direction.	47
3.6	Zoom representation of TAWSS contours of venous anastomosis area.	49

3.7	Zoom representation of OSI contours of venous anastomosis area. . . .	50
3.8	Zoom representation of RRT contours of venous anastomosis area. . .	50
3.9	Contour levels corresponding to 20th and 10th percentile TAWSS values.	51
3.10	Contour levels corresponding to 80th and 90th percentile OSI values. .	52
3.11	Contour levels corresponding to 80th and 90th percentile RRT values.	53
3.12	Visualization of ROI.	54
3.13	Contour levels of TAWSS in region of interest.	56
3.15	OSI contour levels in region of interest.	57
3.14	TAWSS percentile values levels in ROI.	57
3.16	OSI percentile values levels in ROI.	58
3.17	RRT contour levels in region of interest.	58
3.18	RRT percentile values levels in ROI.	59
3.20	WSS-based descriptors mean values and standard deviations.	61
3.19	Histograms of OSI values distribution in region of interest.	62
3.21	Percentage variations vs. Base of WSS-based descriptors mean values.	63
3.22	Iso-surfaces of time-averaged LNH for the eight simulated models, adopt- ing a threshold value equal to ± 0.4	64
3.23	Iso-surfaces of time-averaged LNH for the eight simulated models, adopt- ing a threshold value equal to ± 0.7	65
3.24	Iso-surfaces of LNH at peak systolic time instant, adopting a threshold value equal to ± 0.7	67
3.25	Quantitative helicity descriptors.	68
3.26	Localization of recirculating flow volume in all simulated models. . . .	70

List of Tables

1.1	Stages of Chronic Kidney Disease	9
2.1	Geometric features of flow divider inside AVG models	26
2.2	Meshes set for sensitivity study of AVG base model	28
2.3	Characteristics of AVG models grids	31
3.1	Percentile values of WSS-based descriptors in ROI-1 and ROI-2.	54
3.2	ROI surface area exposed to low TAWSS, high OSI and high RRT.	60
3.3	Percentage of volume involved in recirculating flow.	69

Chapter 1

Introduction

In the first part of Chapter 1, a general introduction of cardiovascular system is reported. Moreover, a summary of pathophysiology involved in kidney failure is illustrated. In the second part of this chapter, peripheral vascular accesses used to have an efficient hemodialysis are surveyed. Focusing on a specific type of vascular accesses, the arterio-venous grafts, it is esplicated their use limitation and the major mechanism involved in their failure. Following, it is possible to find a state of art of researches carried out to investigate and avoid arterio-venous grafts failure by improving the performance of commercially available prosthetic grafts. In conclusion, the preset goal of this work has been explained.

1.1 Cardiovascular system

Cardiovascular system is composed by the heart, the blood vessels and the blood flowing into them. Circulatory system splits into two sub-systems: the systemic circulation and the pulmonary circulation. The heart is a four-chambered pump that distributes the blood to the vessels. Blood is ejected from the right ventricle in the pulmonary artery, in which obtaining oxygen from the lungs, and returns to the left atrium via the pulmonary veins. Through systemic circulation, oxygenated blood has been transported to the rest of body: it is ejected from the left ventricle into the aorta and returns deoxygenated via the inferior and superior vena cava to the right atrium (Figure 1.1).

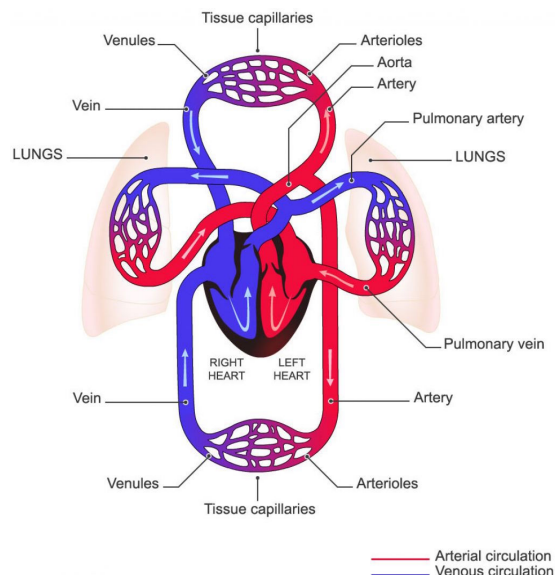


Figure 1.1: The circulatory system: oxygenated blood flow in arteries while deoxygenated blood returns to the heart through the veins.

1.1.1 Blood vessels

Blood vessels are the body's ways that allow blood to efficiently flow from the heart to every region of the body and back again. Firstly, they are distinguished in arteries, that carry blood, under high pressure, with its nutrients and oxygen, to body tissues, and veins, in which blood flows back to the heart. Moving away from the heart, vessels progressively branch and their diameter decreases. Blood

vessels, usually, have three distinct layers: the tunica intima, the tunica media and the adventitia.

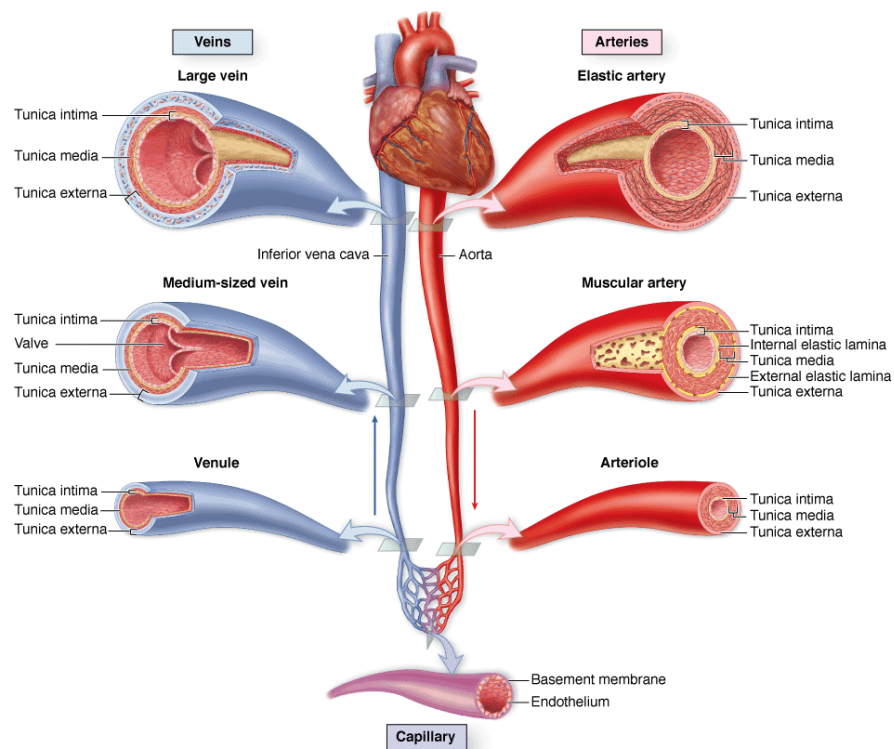
1.1.2 Arteries

According to their dimensions, arteries are classified in:

- large diameter or elastic arteries;
- medium diameter or muscular arteries;
- arterioles, with are less than 2 mm in diameter;
- capillaries, the site of exchange between blood and surrounding tissue.

In the arteries, the innermost layer, the tunica intima, is formed from a single layer of endothelial cells (EC). EC layer is the single barrier between blood and thrombogenic tissues. The intima is separated from the media by an internal elastic lamina (IEL), the most external component of the intima. This lamina, composed of elastin, is fenestrated to allow the diffusion of substances to nourish cells deep in the vessel wall. Furthermore, through these holes, smooth muscle cells of tunica media can penetrate the tunica intima. The tunica media is composed of vascular muscle cells (VSMC) and extracellular matrix (ECM). VSMC are responsible for vessels dilatation and constriction. They also synthesize collagen, PGAG and elastin which establish the mechanical behaviour of the vascular wall. In arteries, the media has a thinner external elastic lamina, which separates it from the tunica adventitia. Finally, the adventitia contains fibroblasts, ECM, nerves and vasa vasorum. The external elastic lamina is fenestrated and, during atherosclerosis process, vasa vasorum of the adventitia can penetrate to the media causing a structural weakening of the vascular wall.

Large arteries include the aorta, the subclavian, the origin of pulmonary arteries and the beginning of the common carotid artery. Elastic arteries have a thicker intima than the corresponding tunica of a muscular artery. Also the tunica media has a different composition in the distinct parts of the vascular tree. In particular, tunica media of large arteries consists of fenestrated elastic laminae alternating



Source: Mescher AL: Junqueira's Basic Histology: Text and Atlas, 12th Edition: <http://www.accessmedicine.com>
Copyright © The McGraw-Hill Companies, Inc. All rights reserved.

Figure 1.2: Representation of blood vessels: large elastic arteries leave the heart and branch to form muscular arteries. These arteries branch further and enter organs, where they branch much further to form arterioles and then capillaries. Blood returns back to the heart through venous system, which increases its diameter by moving from capillaries to large vein.

with collagen fibers and smooth muscle cells. In the small arteries, the tunica media consists mainly of muscle cells, which are wrapped in a spiral fashion with a variable pitch, and a small quantity of elastin and collagen. In arterioles, the subendothelial layer is very thin, the elastic laminae are absent and the media is generally composed of circularly arranged smooth muscle cells. In both small arteries and arterioles, the tunica adventitia is very thin and inconspicuous. Capillaries are composed of a single layer of endothelial cells rolled up in the form of a tube and the basement membrane. Because of their thin walls and slow blood flow (0.3 mm/s), capillaries are a favorable place for the exchange of water, solutes, and macromolecules between blood and tissues.

1.1.3 Veins

Venous system includes, from the smallest to the largest diameter, venules, medium-sized veins and large veins. They consist of three layers, tunica intima, media and adventitia, but the wall thickness of veins is much less than that of arteries, because of its lower pressure than the arterial system. Therefore, blood entering veins moves toward the heart by contraction of the tunica media and external compressions from surrounding muscles and other organs. The intima, usually, has a thin subendothelial layer and the media consists of small bundles of smooth muscle cells intermixed with reticular fibers and a delicate network of elastic fibers. The adventitial layer is thicker than the tunica media and the elastin/collagen ratio is small compared to arteries. This makes veins relatively stiff when fully distended, but when veins are under low or negative pressure they may collapse. Unlike the arteries, intermediate sized veins contain uni-directional valves, which prevent blood from flowing back down.

1.1.4 Blood

Blood tissue consists of a suspension of different particles in an aqueous solution, called plasma. Plasma is a slightly alkaline fluid consisting of 90% water and 1% electrolytes. The majority of molecules that are in the plasma are globulins, albumin and fibrinogen.

The principle particles in blood are red cells or erythrocytes. The red cell has a biconcave shape with a diameter of 8 μm . They are bounded by a membrane, called stroma, which is sensitive to mechanical stresses. Very high mechanical stresses cause the rupture of red cell membrane, a phenomenon called hemolysis, or it can undergo an acceleration of the aging process. These cells are involved in the transport of oxygen from the lungs to the tissues. 90% of the protein content in a red cell is made up of hemoglobin that reversibly link oxygen molecules. The percent by volume of red cells is called the haematocrit (Ht); the haematocrit has a range of 38-52% in healthy men and 36-46% in healthy women. It can also be very high in newborns and in high-altitude populations, while it is low in subjects with anemia or thalassemia. Inside blood vessel, red cells are distributed uniformly and are separated thanks to the negative charge on their membranes. Instead, for low shear rate values of blood flowing, erythrocytes tend to aggregate in rouleaux. This is usually observed in microcirculation; moreover, the aggregates are in the lumen of vessel and rarely close to the wall.

Other particles that make up the blood are white cells or leukocytes. They occupy some 0.7 % of the blood volume in health. They are involved in the immune system. Leukocytes are divided into three groups:

- Monocytes;
- Lymphocytes;
- Granulocytes, that include eosinophils, basophils and neutrophils.

Monocytes are precursors of macrophages. After maturation of monocytes, they are released into blood circulation, they migrate into the connective tissue where become macrophages and then move towards body tissues. Their function is not only the phagocytosis, but also secrete defensive substances. Lymphocytes attack invading bacteria and viruses and also help destroy cells in the body which have become diseased through virus infection or cancer. Eosinophils attack larger parasites and are involved in allergic responses. Basophils secrete anticoagulants or vasodilators substances, such as histamine and serotonin. Neutrophils ingest and digest bacteria.

Platelets are spherical particles with a diameter of 3 μm and they occupy 0.3% of the blood volume in health. Platelets are involved in blood clotting and in the repair of damaged endothelium. They can also be activated by increases in wall shear in narrowed vessels. In hemostasis phenomenon, platelets are involved in three stages: the adhesion to the damaged endothelium, the activation of receptors and secretion of chemical messengers and, at last, the aggregation of platelets through receptor bridges.

1.2 Kidney failure

Blood plasma is filtered by two organs, the kidneys, removing substances from the filtrate at variable rates, depending on the needs of the body, and excreting them in the urine, while substances that are needed return back to the blood [3]. If the kidneys are unable to eliminate waste products from the blood and the condition is untreated, waste substances and fluid build up in the blood, but these are toxic for the body. Kidneys diseases are among the most important causes of death and morbidity in many countries throughout the world. Kidney failure can be of two types:

1. Acute kidney injury (AKI), that is a sudden loss of kidney function and can be reversible;
2. Chronic kidney disease (CKD), that is a progressive loss of function of more and more nephrons that gradually decreases overall kidney function.

1.2.1 Acute kidney injury (AKI)

The causes of Acute Kidney Injury are commonly categorized into prerenal, intrinsic, and postrenal.

Prerenal causes of AKI are those that decrease blood flow to the kidney and cause a drop of Glomerular filtration rate (GFR). GFR is an index of level of kidney function and is defined as the volume of glomerulus filtered fluid into the Bowman's capsule per unit time. It is measured in units of volume per time, e.g., milliliters per minute (ml/min). Prerenal causes include low blood volume due

to severe dehydration, low blood pressure, heart failure and liver diseases.

Intrinsic causes can be due to one or more of kidneys structures such as glomeruli, kidney tubules (tubular necrosis), or the interstitium. Other causes are vascular diseases, e.g. renal artery obstruction and renal vein obstruction.

Postrenal causes are due to an acute obstruction that affects the normal flow of urine out of the kidneys. Main causes are kidney stones, obstructed urinary catheter, bladder stones or cancer of the bladder, ureters or prostate.

Treatment of AKI depends on the cause and can be dialytic or non-dialytic. In the latter case, the aim is to inhibit injury or enhance repair. Hemodialysis can be applied intermittently or continuously.

1.2.2 Chronic kidney disease (CKD)

Chronic kidney disease is a progressive damage of kidney function. It is distinguished from acute kidney disease because of the reduction in kidney function must be present for over 3 months. CKD affects 5–10% of the world population. In general, chronic renal failure, like acute renal failure, can occur because of disorders of the blood vessels, glomeruli, tubules, renal interstitium, and lower urinary tract, but the end result is always a decrease in the number of functional nephrons. The main causes of CKD are diabetes mellitus and hypertension. GFR is used to know the progress of pathology. According to the National Kidney Foundation (NKF), there are five stages of CKD; they are described in the Table 1.1.

Table 1.1: Stages of Chronic Kidney Disease

Stage	GFR (mL/min/1.73 m ²)	Description
1	≤ 90	Kidney damage with normal or \uparrow GFR
2	60 - 89	Kidney damage with mild or \downarrow GFR
3	30 - 59	Moderate \downarrow GFR
4	15 - 29	Severe \downarrow GFR
5	<15 (or dialysis)	Kidney failure

Stage 5 is also called End Stage Renal Disease (ESRD). Treatments for this stage are dialysis, that is a renal replacement therapy, or kidney transplant.

There are three types of dialysis:

- *Hemodialysis*, which is described in the following section;
- *Peritoneal dialysis*, that is a treatment in which peritoneum is used as membrane through which fluid and dissolved substances are exchanged with the blood;
- *Hemofiltration*, that is similar to hemodialysis but dialysate is not used: a pressure gradient is applied that moves water and solutes across the filter membrane from the blood compartment to the filtrate compartment.

1.3 Hemodialysis

Hemodialysis consists of cleaning blood outside the body through a device, called ‘artificial kidney’ or dialyzer. The basic principle is to pass blood through minute blood channels bounded by a thin membrane. On the other side of the membrane is a dialyzing fluid into which unwanted substances in the blood pass by diffusion, while blocks plasma proteins. The rate of movement of solute across the dialyzing membrane depends on (1) the concentration gradient of the solute between the two solutions, (2) the permeability of the membrane to the solute, (3) the surface area of the membrane, and (4) the length of time that the blood

and fluid remain in contact with the membrane [3]. In the extracorporeal circuit, the dialysate flows in the opposite direction of blood flow. Then, the filtered blood returns into the patient's bloodstream through 'venous line' (Figure 1.3). Dialysis machine makes also a series of checks in order to maintain the correct pressure, temperature and composition of dialysate or verify that no air bubble is cretaed in the blood.

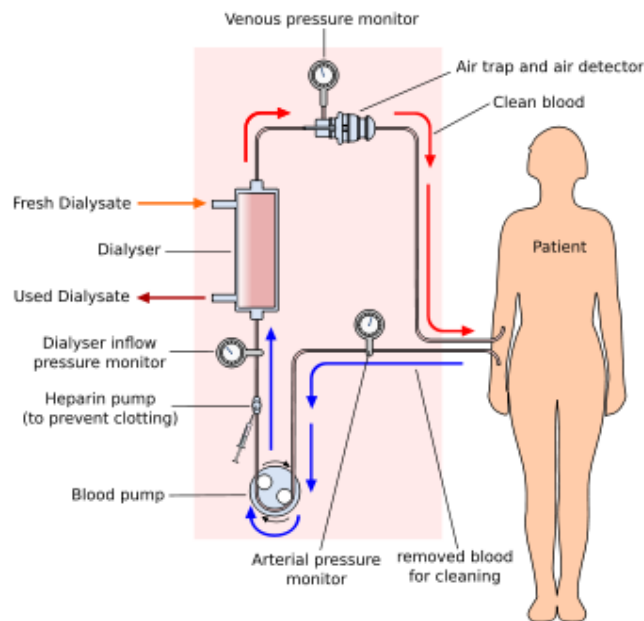


Figure 1.3: Hemodialysis circuit

1.4 Vascular accesses

A fundamental requirement for an efficient hemodialysis is a vascular access. In order to have an efficient flow of blood from patient's vessel to dialyzer, a high flow rate, in a range of 300-500 ml/min, and an high pressure of blood are necessary.

Arterio-venous access types are:

- Venous catheter;
- Autogenous fistula;
- Non autogenous fistula: arterio-venous graft.

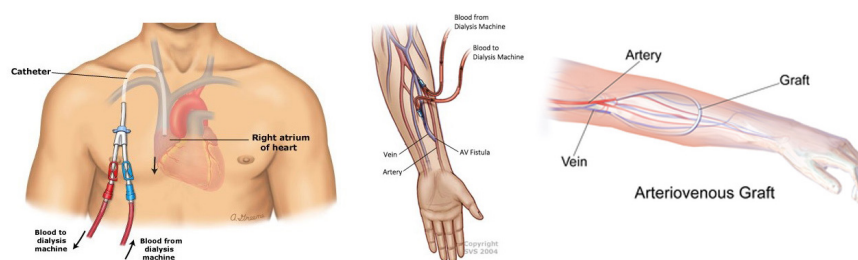


Figure 1.4: Types of vascular access: venous catheter, autogenous fistula and arteriovenous graft.

The choice of access depends on stage of patient's renal failure and the condition of his vessels. To create all of these types of access surgery is required.

A venous catheter is a tube inserted into a vein in the neck, chest, or leg near the groin, usually only for short-term hemodialysis. The tube splits into two when it exits from the body: one is connected to the line that carries blood to dialyzer and the other is connected to the line that carries blood back to the body.

In 1966 Cimino and Brescia performed the first endogenous arterio-venous fistula. In an autogenous fistula, an artery and a vein are surgically joined with one of these four type of anastomosis (Figure 1.5):

- A. Side artery to side vein anastomosis;
- B. End artery to end vein anastomosis;
- C. Side artery to end vein anastomosis;
- D. End artery to side vein anastomosis.

The surgeon usually places an AV fistula in the forearm or upper arm, usually non-dominant arm.

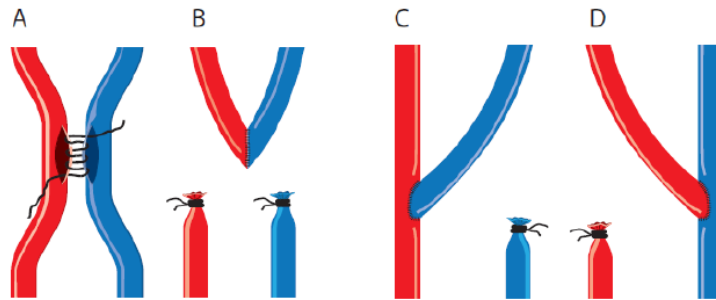


Figure 1.5: Four different anastomotic configurations: A) Side-to-side anastomosis, B) End-to-end anastomosis, C) End-to-side anastomosis, and D) Side-to-end anastomosis

1.4.1 Arterio-venous graft

For patients with inadequate superficial veins, such as elderly and diabetics patients, it is not possible to create an arteriovenous fistula and not-autogenous arteriovenous graft (AVG) is chosen as vascular access [4]. This vascular access is the secondary surgeons choice because of more complexity of operation and it is associated with a greater morbidity than with the autogenous AV fistula.

A prosthetic AV graft can be biological or synthetic. The first are of limited availability, expensive and of variable size. The commonly used are synthetic grafts. The most used material for AVG creation is PTFE, a fluorocarbon polymer which presents a lower risk of disintegration with infection, low thrombogenicity, low tissue reactivity, prolonged patency and improved surgical handling [5]. All graft types can be placed in a straight or loop configuration either in the forearm or in the upper arm; patency of the loop graft configuration is higher than for the straight. The common anastomotic configurations of AVG in the upper limb are: curved brachio-axillary (brachial artery - axillary vein), looped axillo-axillary (axillary artery - axillary vein), forearm looped brachio-basilic (brachial artery - basilic vein), straight radial to cubital fossa vein (Figure 1.6 a-b-c-d). In the lower extremity the vascular access conduit can either be in a straight or a looped configuration and the blood vessels involved are the great saphenous vein anastomosed in an end-to-side fashion to superficial femoral artery or to the popliteal artery (Figure 1.6 e-f) [6].

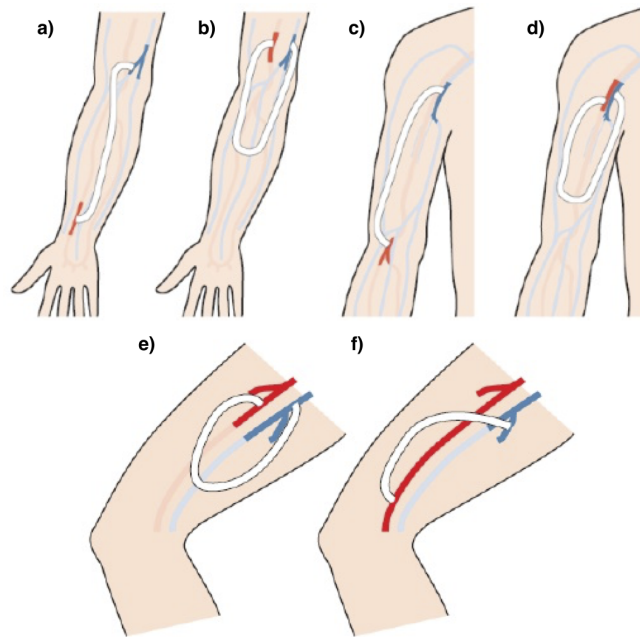


Figure 1.6: Prosthetic graft configurations in the upper and lower extremities: **a)** curved brachio-axillary, **b)** looped axillo-axillary, **c)** forearm straight brachio-basilic, **d)** looped radial to cubital fossa vein, **e)** looped saphenous vein-femoral artery, **f)** straight saphenous vein-femoral artery.

When a fistula is created or an AV graft is implanted, surgical area undergoes a remodeling. The ‘maturation time’ is lower in AVG, about 2-3 weeks, than in AVF, that is about 1-3 months. Before of this period, it is not possible using these accesses for hemodialysis.

1.4.2 Complications of vascular accesses

Both infectious and noninfectious complications affect vascular access and they are associated with increased morbidity, mortality, costs, and a reduced patient quality of life. The main complications of AVF and AVG are of hemodynamic nature, such as:

- thrombosis;
- stenosis;
- aneurysm formation;

- ischaemia;
- heart failure;

Thrombosis

Thrombosis, that appears in the first few months, is due to surgery errors, but the interest of this study is focused on thrombosis that onsets at a later lifetime of vascular access. The main cause of over long time thrombosis is stenosis.

Stenosis

The favorite AVF sites where stenosis occurs are anastomosis area and the draining vein, while in AVG stenosis are situated in venous anastomosis and in the draining vein. This is due to an alteration of venous flow because, after the creation of a vascular access, veins are exposed at different hemodynamics. Infact, at normal condition, pressure is about 20 mmHg, Wall Shear Stress is below 0.76 Pa and flow is not pulsatile. The underlying mechanism of stenosis formation is intimal hyperplasia (IH). IH is initiated by injuries which occur at vessel wall, due to incisions and sutures, and it develops because many factors occur, such as cyclic stretch, abnormal WSS values, the high venous pressure, elastic property mismatch between the graft and the blood vessels and the angle between the graft (or artery) and the vein.

Aneurysm

Aneurysm within the VA conduit, that is an enlargement of the vessel diameter, can be induced by elevated intraluminal pressures in combination with a weakened venous wall. Both AVF and AVG are subject to aneurysm formation because of the repetitive cannulation. Stenotic deformations in the venous outflow are often responsible for the increase in luminal pressure. Therefore, treatment of the stenosis might stop aneurysm expansion. Moreover, aneurysms in VA are at risk for thrombosis due to high residence time of blood and accordingly higher risk of platelet aggregation.

Ischaemia

Ischaemia is due to the inhibition of blood supply to the tissues distal to vascular access. This risk especially occurs when AVG are implanted in the elbow region or within diabetics, as they typically suffer from peripheral vascular disease.

Heart failure

Heart failure is also a common problem in the end stage renal disease (ESRD) population. Creation of an AVF results in a decrease of the peripheral vascular resistance with a subsequent acute and prolonged increase of cardiac output. Studies have confirmed that functional AVFs potentially contribute to the development of cardiac failure by provoking a disbalance between oxygen requirement and oxygen delivery to the myocardium [7].

1.5 Intimal Hyperplasia: the cause of vascular access failure

The intimal hyperplasia (IH) is a process, during which the inner layer of a blood vessel, the tunica intima, has a thickening due to migration of vascular smooth muscle cells (VSMC) from the media to the intima. Polytetrafluoroethylene (PTFE) grafts can induce the production of VSMC growth factors in several ways [8]:

- activation of macrophages, which excrete growth factors as a result of foreign body response;
- uncovered PTFE activates platelets which can release growth factors;
- compliance mismatch at the anastomosis may lead to excessive stretching of the VSMC, inducing the VSMC to proliferate;
- turbulence which occurs around the anastomosis causes endothelial cell damage and release of growth factors;

- zones of low shear and flow separation present around the anastomosis cause platelet adherence and activation.

The pathogenesis of neointimal hyperplasia in AVG stenosis is commonly divided into upstream and downstream events. When the graft is inserted in vessels, the hemodynamics changes and disturbed flow causes injuries to endothelium (upstream event). Normal endothelium produces VSMC proliferation-inhibiting factors, such as nitric oxide (NO), but this is reduced when endothelium is damaged. When the endothelium is injured, endothelial cells, which act as mechanotransducers, release inflammatory mediators that trigger platelet aggregation, fibrin deposition and recruitment of leukocytes to the area (downstream events). These cells express growth factors that promote smooth muscle cells migration from the media to the intima. The smooth muscle cells proliferate in the intima and deposit extracellular matrix, in a process analogous to scar formation. The neointimal SMC proliferate for up to 2 weeks [9].

1.5.1 Hemodynamics and intimal hyperplasia

It is acknowledged that Wall Shear Stress is a determinant factor in the release of vasoactive compounds from the endothelial cells. Wall shear stress is related to flow and inversely related to diameter. From the hemodynamic point of view, when a vein is connected to an artery, venous flow increases, but so does the diameter. Since the influence of diameter is superior, the shear stress will usually be lowered. Vessels respond to reduced shear stress by constricting. This is to be attributed to endothelial cells. In rigid PTFE grafts where vasoconstriction cannot occur, the endothelial cells attempt to maintain shear stress within the physiological range increasing intimal thickening [8].

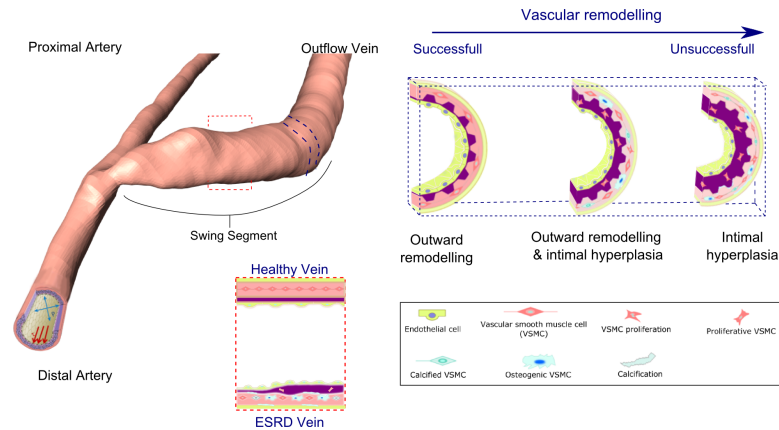


Figure 1.7: Vessels remodelling and onset of Intimal hyperplasia

1.6 A literature review

The development of IH in a vascular access mostly occurs in venous segment of the access. Many researches have been conducted in the past few decades to design grafts with longer patency, ideally longer than the life-span of the patient.

1.6.1 Bulk flow

In the last years, it has been observed that intravascular structures, too, contain important informations in order to understand the mechanism of vascular diseases. In hemodynamics, geometry shapes the flow. Vasculature, at the level of large and medium-size arteries, has curved structures with no trivial torsion. This complex geometry promotes helical flow, that is, 3D in plane flow. Helical patterns have been observed in areas from the ascending aorta to the aortic arch during the systole. Specifically, the upper aortic arch of the healthy subjects during late systole exhibits a single right-handed helical flow which is different from the symmetrically paired and counter-rotating helices (Dean flow pattern) developing at a simple pipe bend. It has been observed that helical flow also exists in human infrainguinal blood vessels and in pulmonary circulation [10]. Helical flow, within a physiological range, has several positive roles:

- from the physiological point of view, it allows greater organ perfusion. In fact, the higher the vorticity of the flow of descending aorta, the higher the

blood flow to the tissues.

- spiral-shaped flow allows greater mixing of oxygen and nutrients carried by blood.
- it inhibits the transfer of energy from larger to smaller scales, where it is dissipated. It was demonstrated that the rate of Kolmogorov spectrum formation is diminished by the helicity.
- it has a wall wash out effect, so it prevents generating considerable flow separation areas.

In the past, the potential role of bulk flow in the development of vasculature disease was of little interest for researchers. Morbiducci et al. [11] discovered a linear inverse relationship between helical flow structures and vascular wall indexes, in particular the magnitude of oscillating shear stress, in aortocoronary bypass models. The helical flow has been introduced to the design of vascular interventions, such as arterial bypass graft and artero-venous graft to reduce the thrombus formation and intimal hyperplasia caused by the abnormal flow conditions.

1.6.2 Researches enhancing AVG patency

Many AVG geometries have been tested during last decades, in order to improve local induced hemodynamic features and establish a favorable laminar flow pattern, which in theory should avoid or, at least, reduce the development of IH. For this purpose, a cuffed graft, VenaflowTM (Bard Peripheral Vascular), has been realized. VenaflowTM graft has a cuff at its venous anastomotic side. An in vitro study of Heise et al. [12] explores, using Particle Image Velocimetry (PIV), the hemodynamics associated with cuffed and straight PTFE-venous anastomoses. Results from this study highlight that shear stresses at the venous floor in the Venaflow graft are much lower compared to straight AVG. The higher wall shear stress areas near the venous floor for the straight configuration are correlated to regions of maximum IH development. Therefore, Heise supports the hypothesis that venous remodelling results from high-shear flow leading to the hyperplastic

response of the vessel wall in order to prevent its rupture, unlike the proliferative response of the arterial wall to low-shear. Furthermore Heise et al. conducted an in vivo animal study [13] in which analyze two groups of AVG, one straight and one cuffed, following the explant. This study stated that short-term patency rate of Venaflo-type grafts is superior, but a significant pseudointima leading to subtotal graft stenosis was observed in both AVG types. Therefore, the long-term prognosis of cuffed grafts is still very limited, since the grafts start to fail after a delayed time.

Conventional straight AVG graft has also been compared with tapered grafts. Many studies have been conducted in this sense. Among them, Sarmast et al. [14] highlighted that tapered 6- to 8-mm AVG outperforms hemodynamically straight 6-mm graft, thanks to greatly reduced magnitudes of hemodynamic indices associated with less disturbed flow patterns at venous anastomosis.

To date, helical AVG commercially available is the SwirlGraft (Veryan Medical), developed by Caro and made up according to the Small Amplitude Helical Technology (SMAHT). Caro et al. [15] effectuated a comparative study between the SwirlGraft and a conventional ePTFE carotid artery-to-jugular vein shunt. Model studies suggested a lesser pathology in the SwirlGraft AV grafts than in the conventional AV shunts which is visible at eight weeks. Furthermore, numerical simulations lead to the expectation of swirling flow, in-plane mixing, relative uniformity of wall shear, and inhibition of flow stagnation, separation and instability in the SwirlGraft devices and graft–vein junctions.

Van Kanneyt et al. [16] studied the occurrence of unfavorable hemodynamic conditions at the venous anastomosis of five helical designed grafts, which differ for helical pitch. Results of this study are not trivial to interpretate, but the model with the smallest helical pitch seems to present the best hemodynamic features in terms of high and not oscillating shear stress and counter rotating structures more intertwined.

Another AVG commercially available is the Spiral Flow Graft produced by Vascular Flow Technologies, which presents at distal end of graft a spiral flow inducer segment in order to restore normal blood flow, that is spiral laminar flow. A comparative study is conducted by Kabinejadian et al. [17], which carried out

numerical simulations for four end-to-side distal graft anastomosis to assess the effects of inducing secondary flow, which is believed to remove unfavourable flow environment. The first model represents a conventional end-to-side distal graft anastomosis for a peripheral artery bypass configuration. The second model has an internal spiral inducer in the form of an internal ridge, that reproduces the commercial Spiral Flow Graft; the third is in a helical configuration and reproduces the commercial SwirlGraft; the last is a combination of helical and spiral geometries. This study demonstrated that, to have swirling flow in the anastomosis, the helical geometry is more effective than the spiral ridge geometry and the combination of two geometries enhanced swirling flow, with predominantly single vortex and asymmetrical distributions of velocity and WSS parameters.

In a recent study of Kabinejadian et al. [18], a new anastomosis geometry is realized in order to enhance graft patency, that is coupled sequential anastomoses (CSQA). This type of anastomosis consists of a side-to-side anastomosis and a end-to-side anastomosis downstream of the first. Dividing the flow between two venous anastomoses, it's possible to reduce the WSS at each junction by enhancing the AVG patency.

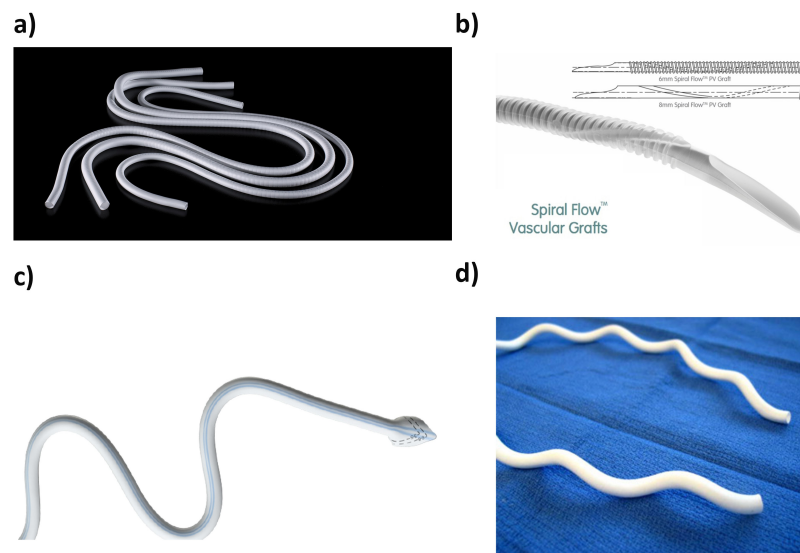


Figure 1.8: Arterio-venous grafts commercially available. **a)** Straight conventional graft, **b)** Spiral Flow graft 1, **c)** Cuffed arterio-venous graft [2], **d)** Swirl graft (Veryan Medical).

1.7 Research goal

The primary cause of arterio-venous grafts failure is stenosis due to neointimal hyperplasia, which limits their use, resulting in arterio-venous fistula in the forearm to remain as an ideal vascular access for patients undergoing haemodialysis. The failure rate of a vascular access varies between 18 to 28% for AVF and higher for AVG [19]. Hemodynamics is believed to play a role in this process. It has been demonstrated that the spiral flow is a physiological feature which occurs in the whole arterial system and is induced by the twisting of the left ventricle during contraction and is supported by the tapered, curved and non-planar geometry of the arterial system. Therefore, many studies have been conducted to design and create a vascular access, promoting physiological blood flow establishment and limiting or avoiding unfavorable hemodynamics which could contribute to vascular graft failure. However, clinical evaluation of new proposed grafts has not shown great benefits on graft patency with respect to standard AVGs. In this context, the aim of this study is to investigate the impact on hemodynamics of six novel designs of AVG. More in detail, six novel geometries of arterio-venous graft are modelled, and their efficiency in preventing neointimal hyperplasia at the venous anastomosis is tested and compared to two commercially available AVG models. The model resulting in the lowest surface area exposed to unfavorable hemodynamic conditions is proposed as the AVG design potentially decreasing the insurgence of neointimal hyperplasia at the investigated site and improving clinical performances of AVG, as vascular access.

Chapter 2

Materials and methods

In this chapter, geometrical characteristics of created AVG models are described. The second steps is to describe characteristics of computational mesh and the method used to choose, from a set of grids, the one that balances accuracy solution and computational and memory costs. Then, it has been reported setting parameters of numerical unsteady-state simulation. Finally, methods used to perform post-processing analysis has been discussed.

2.1 Arterio-venous graft (AVG) models

In order to investigate local hemodynamics within novel geometries of vascular access, eight models of AV graft are created in Solidworks®. All of patterns consist of a looped graft with a diameter of 6 mm and length of 300 mm. The AV graft connects an artery of 4 mm of cross-section diameter with a vein of 6 mm. Vessels are modelled as cylindrical conduits with a length of 90 mm. The surgical connection between the graft and the vessel is called anastomosis. In these models, grafts are connected to vessels by an end-to-side anastomosis, that forms two angles of 45° , with the artery and the vein respectively; thus, it is possible to identify five areas:

- **GRAFT**, that is anastomosed with the artery and the vein;
- **Proximal artery (PA)**, that is upstream of arterial anastomosis;
- **Distal artery (DA)**, downstream of arterial anastomosis;
- **Proximal vein (PV)**, downstream of venous anastomosis;
- **Distal vein (DV)**, upstream of venous anastomosis.

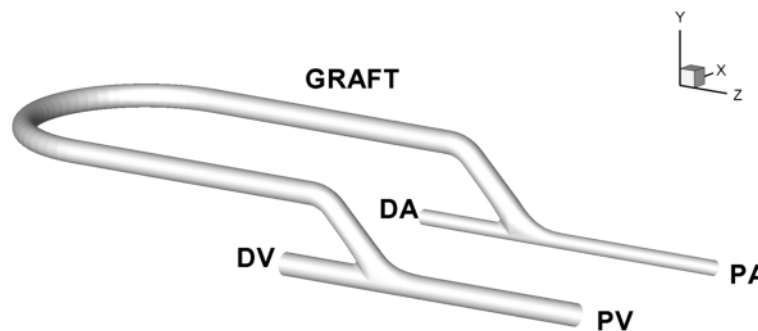


Figure 2.1: Base arterio-venous graft model anastomosed to an artery and a vein. Vessels are divided in a proximal zone, in which flow normally, while in distal section a small flow rate is sent.

The base and helical models have been made up to have a comparison. Novel design models have been created from Base model design, in which a flow divider

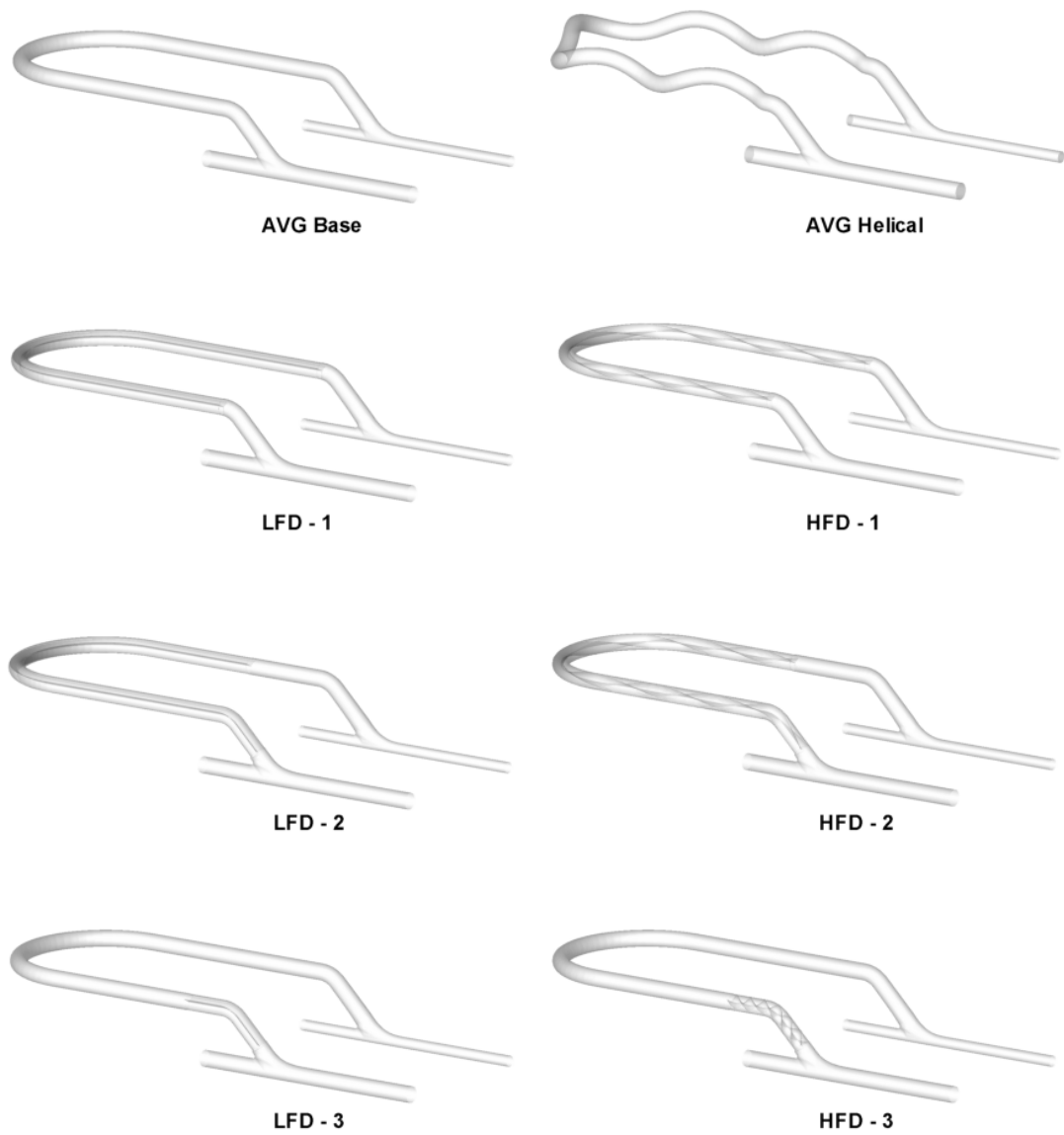


Figure 2.2: AVG models: AVGs Base and Helical doesn't have flow divider, while AVGs LFD and HFD have flow divider witch differs for its position (1-2-3) and its helical pitch (HFD).

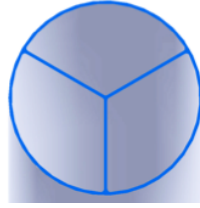


Figure 2.3: Cross-section of flow divider

is inserted. Flow divider separates the conduit of graft in three parts, according to Figure 2.3. Three positioning of the flow divider inside the vascular access have been tested and for each model two flow divider configurations have been simulated: one linear and one helical. In the linear configuration, flow divider conduits are fixed, while in the helical configuration they rotate around the axis of the graft to form three helical channels. In particular, in models LFD-1 and HFD-1, the flow divider starts at the end of the curved arterial side of AVG and it ends at the beginning of the curved venous side of AVG. It has a length of 250 mm and, for model HFD-1, the helix pitch is 83 mm. For models LFD-2 and HFD-2, flow divider has a length of 210 mm and it starts 30 mm downstream of the end of curved arterial side of the graft and it ends close to the venous anastomosis. The pitch of helical flow divider inside model is 80 mm. Indeed, the latter models are not reliable, due to the impossibility of inserting the needle of venous line hemodialyzer at venous side of AVG. In models LFD-3 and HFD-3, the flow divider is only of 43 mm: it starts 10 mm upstream of the beginning of the venous curved part and it finishes close to the venous anastomosis. The pitch of HFD-3 model is 21.5 mm.

Finally, a helical model is created. The pitch of external helix is about 50 mm; this value is in accordance to a commercially available arteriovenous graft, the SwirlGraft (Veryan Medical Limited, UK). A summary of models characteristics has been reported in Table 2.1.

Table 2.1: Geometric features of flow divider inside AVG models

Models	Flow divider			
	Length [mm]	Diameter [mm]	Pitch [mm]	Turns
AVG Base	–	–	–	–
AVG Helical	–	–	–	–
LFD-1	250	–	–	–
HFD-1	250	6	83	3
LFD-2	210	–	–	–
HFD-2	210	6	80	3
LFD-3	43	–	–	–
HFD-3	43	6	21.5	2

2.2 Computational mesh

Models are discretized with hybrid grids, generated with ANSYS ICEM CFD v.14.5. Hybrid grids includes tetrahedral elements in the core region and prismatic elements in the boundary layer. Each mesh was created using the Robust (Octree) method, that generates a tetra mesh, and a triangular mesh was used to mesh surface. Then, a boundary layer of prismatic elements is created on existing mesh in order to have a better resolution near the wall of the models. For Base and Helical models, the maximum size of element has been chosen equal to 0.4 mm. Instead, for models with flow divider the maximum element size is equal to 0.2 due to the more complex geometry originated at flow divider section vertices. Size limit of the smallest element has also been chosen, to avoid subdividing elements in a smaller element size than this value. To improve quality of the mesh elements, a smoothing of them has been applied. By choosing an high smoothing iterations, a less number of elements for each iteration have been smoothed. For vascular applications, a mesh having a quality level greater than or equal to 0.3 is defined as a good mesh.

2.2.1 Computational setting for mesh sensitivity

For each model, a mesh sensitivity has been conducted, in order to make results of numerical analysis grid independent. For mesh sensitivity, steady-state simulations have been conducted. Computational set parameters are listed below:

- Steady-state flow condition;
- Blood is set as Newtonian fluid, with density equal to 1060 kg/m^3 and dynamic viscosity equal to 3.5 cP ;
- Boundary conditions: a flat profile of velocity equal to 0.7984 m/s is set in inlet (PA). The velocity value has been computed as the time-averaged velocity taken from a post-operative inflow-rate profile; outlet flows are set as a percentage of the inlet flowrate, in particular, 5% of the inflow rate is sent at DA, 90% of that is sent at PV and 5% at DV. At last, stationary and no-slip condition are fixed for the wall.
- To control solutions, second order for pressure and first order upwind for momentum are established.
- For convergence criterion, residuals are imposed equal to 10^{-4} .
- To control numerical simulation, volume flowrate at inlet and outlets have been monitored.
- The motion variables are initialized at 0 and the number of maximum iterations are set to 2500.

2.2.2 Mesh sensitivity analysis

For the base model, a mesh sensitivity test with eleven grids is implemented. Grids differ for the thickness of boundary layer and the number of layers and they are ordered according to increasing number of prismatic grid cells (Table 2.2).

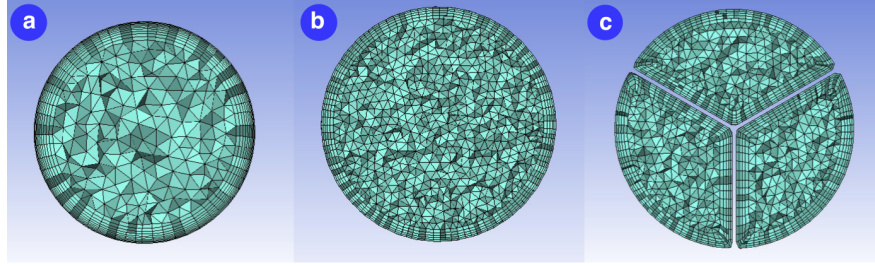


Figure 2.4: Grid with tetrahedral elements in the core region and prismatic elements in the boundary layer. a. Boundary layer thick 0.5 mm and 10 layers.; b. Boundary layer thick 0.3 mm and 5 layers; c. Boundary layer thick 0.5 mm and 10 layers, cross section of flow divider.

Table 2.2: Meshes set for sensitivity study of AVG base model

Grids	Boundary layer		Number of elements	
	Thickness [mm]	Layers	Tetrahedral	Prismatic
Mesh 01	0.5	5	1,741,313	1,135,870
Mesh 02	0.5	5	2,495,556	1,361,635
Mesh 03	0.5	10	1,017,402	1,561,580
Mesh 04	0.5	10	1,366,030	1,764,130
Mesh 05	0.5	5	4,178,284	1,988,800
Mesh 06	1.0	10	1,444,405	2,271,282
Mesh 07	0.5	10	1,747,238	2,271,740
Mesh 08	1.0	10	932,618	2,723,270
Mesh 09	0.5	10	2,499,374	2,723,270
Mesh 10	1.0	10	2,326,571	3,151,300
Mesh 11	0.5	10	3,038,089	3,151,300

and four parameters have been analyzed:

- Maximum velocity;
- Volume averaged velocity;

- Maximum wall shear stress;
- Mean wall shear stress.

In order to make results grid independent, percentage differences of these parameters have been computed with respect to the grid with the more dense boundary layer. Hemodynamic parameters vary more quickly near the wall. The more dense mesh is Mesh 11 in the Table 2.2. Percentage differences of mean WSS in Figure 2.5 highlight that this parameter varies in relation to the thickness of the boundary layer and the number of layers, while grids with the same characteristics have changes, in most cases, less than 1%.

Since the more dense boundary layer is thick 0.5 mm and it has 10 layers, the attention is focused on set of grids having these features (Figure 2.6). Analyzing maximum WSS (Figure 2.7), that presents the highest differences respect to Mesh 11, it is found that Mesh 4 has a smaller change, that is about 4%. Since Mesh 4 has percentage differences of maximum and mean velocity less than 1% (0.9% and 0.25% respectively), it has been chosen to perform unsteady-state simulation. Furthermore, it has only 3,300,000 total elements, thus it has a reduced computational cost.

For the other models, a smaller set of grids has been analyzed. All of grids have a boundary layer thick 0.3 mm with 5 layers. At the same way, the sensitivity study has been carried out computing the percentage variations of maximum and mean velocity and maximum and mean WSS with respect to those of more dense boundary layer. In short, grids with percentage variations less than 1% and with a smaller number of elements have been chosen. In Table 2.3 characteristics of grids have been summarized.

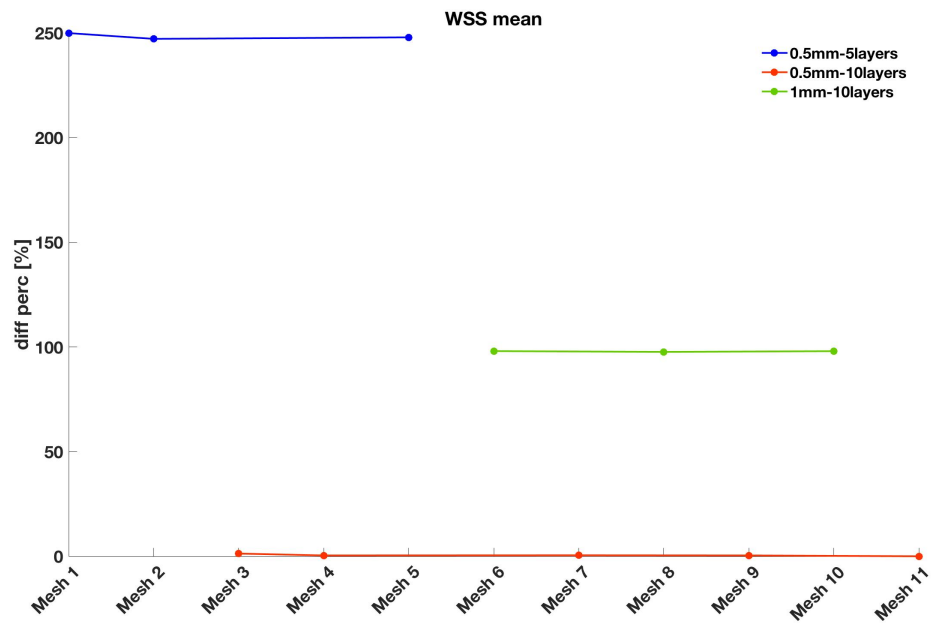


Figure 2.5: Percentage differences of mean WSS of all grids with respect to that of Mesh 11.



Figure 2.6: Percentage differences of mean WSS of only grids with 10 layers and thickness boundary layer of 0.5mm with respect to that of Mesh 11.

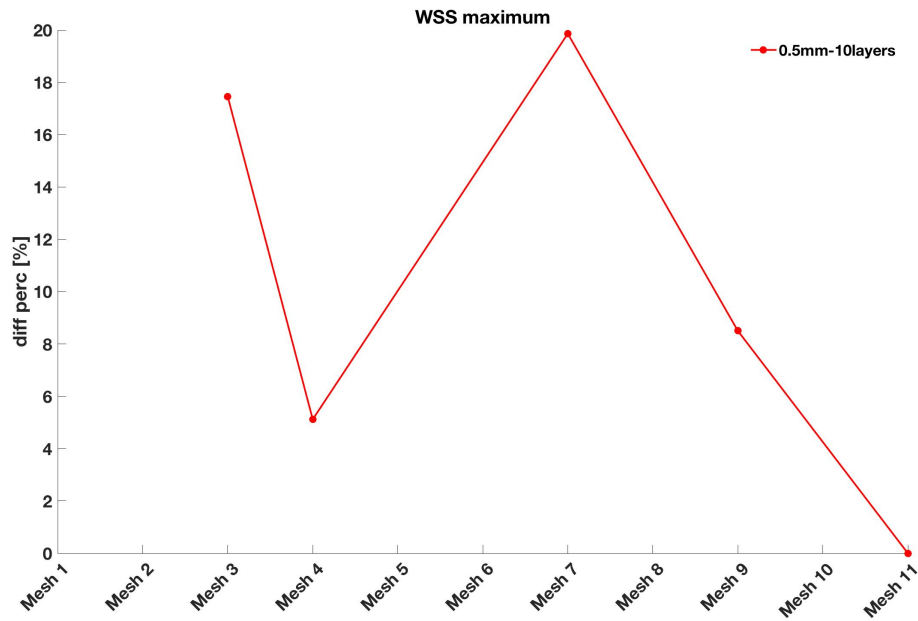


Figure 2.7: Percentual differences of maximum WSS of only grids with 10 layers and thickness boundary layer of 0.5mm with respect to those Mesh 11

Table 2.3: Characteristics of AVG models grids

AVG Models	Boundary layer		Number of elements		
	Thickness [mm]	Layers	Tetrahedral	Prismatic	Total
AVG Base	0.5	10	1,366,030	1,764,130	3,306,573
AVG Helical	0.5	10	1,449,732	1,917,020	3,561,468
LFD-1	0.3	5	7,057,316	3,979,953	11,834,814
HFD-1	0.3	5	7,165,842	4,129,183	12,123,710
LFD-2	0.3	5	7,107,943	3,899,844	11,813,784
HFD-2	0.3	5	7,276,647	3,965,854	12,096,265
LFD-3	0.3	5	7,566,743	2,952,935	11,121,117
HFD-3	0.3	5	7,617,361	2,984,597	11,222,772

2.3 Unsteady-state simulations

Computational fluid dynamics has been carried out by the finite volume package ANSYS Fluent v.6.0.

2.3.1 Governing equations

The fluid dynamics can be described through the conservation laws, in terms of the conservation mass, momentum and energy, along with the continuity equation. There are two methods to observe the fluid flow within some three-dimensional domain that we will denote by R^3 : the Eulerian approach, which consists in observing the fluid velocity at locations that are fixed in space, and the Lagrangian approach, which track specific, identifiable fluid material volumes that are carried about with the flow [20]. In this work, Eulerian approach has been adopted.

The continuity equation states that the rate of change of fluid mass inside a control volume must be equal to the net rate of fluid flow into the volume:

$$\rho \left[\frac{\partial \mathbf{u}_x}{\partial x} + \frac{\partial \mathbf{u}_y}{\partial y} + \frac{\partial \mathbf{u}_z}{\partial z} \right] = 0 \quad (2.1)$$

The continuity equation for a incompressible fluid, where ρ is constant, is given by:

$$\nabla \cdot \mathbf{u} = 0 \quad (2.2)$$

which says that the volume (rather than the mass) of fluid parcels is constant in time.

Conservation momentum law states that the change in momentum of the fluid within a control volume will be due to the following factors:

- the net flow of momentum into the volume;
- the external forces acting on the surface of the control volume;
- the internal volume forces.

Momentum equation can be described as following:

$$\rho \left(\frac{\partial \mathbf{u}}{\partial t} + \mathbf{u} \nabla \cdot \mathbf{u} \right) = -\nabla p + \rho \nabla^2 \mathbf{u} \quad (2.3)$$

where ρ is the density of blood, \mathbf{u} is the velocity vector and p is the static pressure.

2.3.2 Computational setting and boundary conditions

The blood is assumed to be a homogeneous, incompressible and Newtonian fluid with a density of 1,060 kg/m³ and a dynamic viscosity of 3.5 cP. To lead simulations, flow is supposed unsteady. The flat profile of velocity in inlet (PA) has been obtained by a patient specific inflow rate profile (Figure 2.8), previously adopted by Van Canneyt et al.[16], which is reconstructed with the fast fourier transform (FFT). The inflow is split so that 5% of that is sent to distal artery (DA), 5% is sent to distal vein (DV) and the remaining 90% is sent to proximal vein (PV), in accordance with American guidelines. At the arterial, venous and graft walls a rigid and no-slip boundary condition is set.

As for the computational setting, second order pressure discretization and second order upwind momentum discretization scheme have been applied. The residual criterion to ensure the convergence of the numerical method is set to 10⁻⁴. A 1 ms time step and a cardiac cycle period of 1 s have been chosen. In order to eliminate the start-up effects of transient flow, 2.000 time steps are executed. Two heart cycles are simulated this way and the second period results are taken into account. For the second cardiac cycle, one time step in two has been considered in order to reduce memory costs.

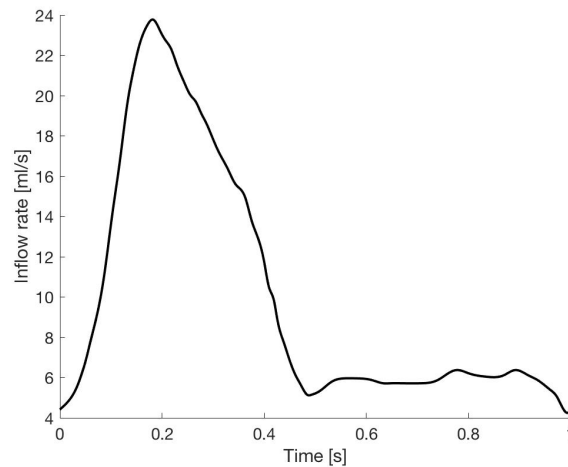


Figure 2.8: Flow waveform of post-operative vascular access patient.

2.4 Methods for analysis

The quantities described below have been computed with Matlab (The Mathworks, USA) and visualized with Tecplot 360 (v. 2009).

2.4.1 Wall Shear Stress

Mainly, phenomena that occur at vessel wall are accountable to the onset of vascular pathology. Two main hypothesis are adopted in literature that link the onset of vascular pathologies to the hemodynamics factors, in particular Wall Shear Stress (WSS):

1. the disturbed shear is recognized in low and oscillating shear;
2. disturbed shear is identified in high shear.

Considering the flow of a fluid in a cylindrical tube, its velocity vary along the radius of conduit. Specifically, it is highest at the center of the tube and decreases toward the wall of tube (Figure 2.9). The velocity gradient is due to frictional forces that are exerted between adjacent layers of the flowing fluid and between the fluid and the walls of the tube, due to viscous properties of the fluid. Wall shear stress in a blood vessel is the force per unit area created when a tangential

force (blood flow) acts on a surface (endothelium). The magnitude of WSS is proportional to the velocity gradient near the wall of the conduit, that is called wall shear rate:

$$WSS = \mu \left(\frac{\partial u}{\partial y} \right)_{y=0} \quad (2.4)$$

where μ is dynamic viscosity of the fluid, u is the axial velocity and y the distance from wall. Shear stress is measured in Pa or dyne/cm² (1 Pa = 10 dyne/cm²).

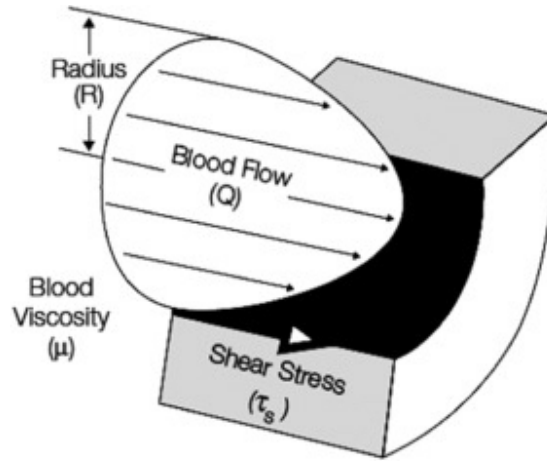


Figure 2.9: Velocity distribution of blood in a vessel

2.4.2 WSS - based descriptors

Since WSS changes during a cardiac cycle, Computational Fluid Dynamics (CFD) calculates wall shear stress values for each node of discretized vessel wall at each cardiac cycle. These values are difficult to reading. Thus, many parameters have been suggested to synthesize informations derived by CFD. WSS-based parameters have been reported below.

Time-Averaged Wall Shear Stress (TAWSS)

TAWSS is indicated as the average of WSS on a period T.

$$TAWSS = \frac{1}{T} \int_0^T |WSS(s, t)| dt \quad (2.5)$$

It is widely accepted that TAWSS values lower than 0.4 Pa stimulate pro-atherogenic endothelial phenotype. TAWSS values between 1.5 and 10 - 15 Pa are considered atheroprotective, i.e. they does not stimulate the onset of pathology, while values higher than 15 Pa are indicative of an endothelium lesion.

Oscillatory Shear Index (OSI)

$$OSI = 0.5 \left[1 - \left(\frac{\int_0^T WSS(s, t) dt}{\int_0^T |WSS(s, t)| dt} \right) \right] \quad (2.6)$$

Oscillator Shear Index identifies regions of the luminal surface subjected to highly oscillating WSS directions during the cardiac cycle [21]. OSI is an adimensional quantity which varies between 0 and 0.5. When OSI=0, it means that WSS never changes direction. It is an indicator of unidirectional flow. OSI=0.5 means that WSS is a cyclic vector. In the latter case, there is no preferential direction of the flow. Therefore, areas in which $OSI \simeq 0.5$ are suggestive of proatherogenic wall regions, while $OSI \simeq 0$ indicates atheroprotective wall regions.

Relative Residence Time (RRT)

Relative Residence Time is a combination of TAWSS and OSI:

$$RRT = \frac{T}{\int_0^T |WSS(s, t)| dt} = \frac{1}{(1 - 2 \cdot OSI)TAWSS} \quad (2.7)$$

This parameter synthetizes information of wall areas where high OSI and low TAWSS occur at the same time, but it is not a robust predictor of low and oscillating shear stress, because TAWSS and OSI have different ranges, between 0 and ∞ and between 0 and 0.5, respectively.

2.4.3 Region of interest

The performance of each design was evaluated by the definition of the surface area at the venous anastomosis subjected to "disturbed shear". In detail, a region of interest (ROI) at the venous anastomosis was isolated. The ROI is extended for

3 venous diameters (i.e. 18 mm) and has an area equal to 90 mm² (Figure 2.10). By pulling data from all the eight simulations, threshold values of unfavorable conditions for TAWSS, OSI and RRT were defined. As in previous studies (Gallo et al., 2012 [22], 2016 [23]), the 20th percentile value for TAWSS and the 80th percentile values for OSI and RRT were estimated. The surface areas (SA) at the defined ROI with OSI and RRT above, TAWSS below, their respective threshold values were quantified.

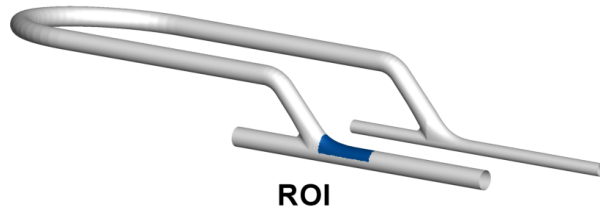


Figure 2.10: Representation of ROI in AVG model.

2.4.4 Helicity

To better understand the torsional phenomena of intravascular structures, a quantity, called density of kinetic helicity, is introduced here. By definition, density of kinetic helicity is the product between velocity and curl of velocity vectors.

$$h(\mathbf{s}, t) = \mathbf{v} \cdot (\nabla \times \mathbf{v}) \quad (2.8)$$

The curl of velocity vector is called vorticity:

$$\boldsymbol{\omega} = (\nabla \times \mathbf{v}) = \begin{bmatrix} \hat{i} & \hat{j} & \hat{k} \\ \frac{\partial}{\partial x} & \frac{\partial}{\partial y} & \frac{\partial}{\partial z} \\ u & v & z \end{bmatrix} \quad (2.9)$$

The direction of the vortex vector detects the spin of the fluid element. Physically, it is the axis around which the fluid element rotates. From the combination of translational and rotational motion, a translated spiral-shaped motion is obtained. Equation 2.8 becomes:

$$h = \mathbf{v} \cdot \boldsymbol{\omega} = |\mathbf{v}| |\boldsymbol{\omega}| \cos(\varphi) \quad (2.10)$$

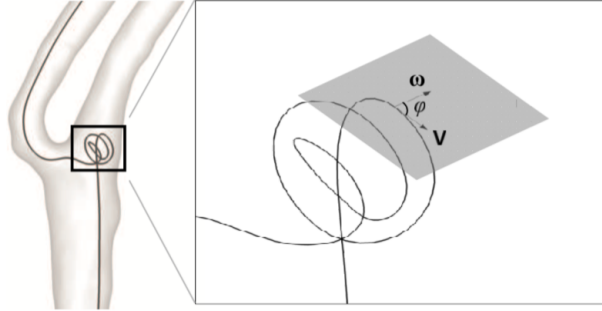


Figure 2.11: Helicity representation [28].

Therefore, helicity is a measure of the alignment of the velocity and the vorticity vectors. When $h=0$, it means that φ is equal to 90° and the observed fluid element rotates with a spin orthogonal to the direction it moves. When φ is equal to 0 or 180° , it means that velocity and vorticity vectors are aligned.

2.4.5 Helicity - based descriptors

Local Normalized Helicity (LNH)

The local normalized helicity is the density of helicity normalized with respect to the velocity vector and vorticity vector modules, corresponding to the local angle between the velocity and vorticity vectors.

$$LNH = \frac{\mathbf{v}(s, t) \cdot \boldsymbol{\omega}(s, t)}{|\mathbf{v}(s, t)| \cdot |\boldsymbol{\omega}(s, t)|} = \cos \varphi(s, t) \quad (2.11)$$

Ranges of this parameter varies from -1 to 1 and its sign is indicative of counter-rotating fluid structures. In particular negative sign denotes left-handed rotation, while positive sign stands for right-handed rotation of fluid domain structures. LNH is equal to 1, in absolute terms, when the flow is exclusively helical, while it is equal to 0 when there is a symmetry of helical structures.

Quantitative helicity indexes

LNH is a qualitative descriptor, which gives a visual indication of complex flow patterns in hemodynamics. To quantify the helical flow structures in terms of strength, size and relative rotational direction, Gallo et al. [22] proposed six different indexes.

$$h_1 = \frac{1}{TV} \int_T \int_V H_k dV dt \quad (2.12)$$

$$h_2 = \frac{1}{TV} \int_T \int_V |H_k| dV dt \quad (2.13)$$

$$h_3 = \frac{h_1}{h_2} \quad (2.14)$$

$$h_4 = |h_3| = \frac{|h_1|}{h_2} \quad (2.15)$$

$$h_5 = \frac{\int_T \int_{V_d} dV dt}{\int_T \int_{V_m} dV dt} = \frac{\max(V_+, V_-)}{\min(V_+, V_-)} = \frac{V_d}{V_m} \quad (2.16)$$

$$h_6 = \frac{1/V_d \int_T \int_{V_d} H_k dV dt}{1/V_m \int_T \int_{V_m} H_k dV dt} \quad (2.17)$$

Where T is the interval of a cardiac cycle, V is the volume of fluid, V_+ and V_- are the total volumes of helical structures rotating in clockwise (positive) or counter clockwise (negative), respectively. While, V_d and V_m are the volumes occupied by the dominant and by the minor direction of rotation of helical structures, respectively. The descriptor h_1 (Eq. 2.12) is the time averaged helicity, normalized with respect to the volume of integration. $h_1=0$ means that symmetric counter-rotating helical structures are present, or when no helicity occurs, in the fluid domain. Instead, when it has a signed value, its sign indicates the predominant direction of rotation. The descriptor h_2 (Eq. 2.13) is given by the integration of absolute value of helicity and it doesn't take into account the direction of rotation, but it is an indicator of the total amount of helical flow in the fluid domain.

Descriptor h_3 (Eq. 2.14), given by the ratio between the first two indexes, is a non-dimensional quantity. It varies between -1 and 1:

- $h_3 = -1$ means that only left handed helical structures are present in fluid domain;
- $h_3 = 0$ means that a reflectional symmetry of helical structure are present;
- $h_3 = 1$ means that only right handed helical structures are present.

Descriptor h_4 , is the absolute value of h_3 , thus its value ranges between 0 and 1. This descriptor neglects what is the main direction of rotation. Descriptor h_5 is the ratio between the volumes of the helical structures in the dominant direction of rotation V_d and the minor direction of rotation V_m , while h_6 is the ratio of helicity intensity in volumes V_d and V_m .

2.4.6 Recirculating flow volume

It is widely observed that many natural and pathological conditions, such as arterial branching and curvature, atherosclerotic plaques, or anastomosed zones cause disturbed blood flow patterns, e.g. flow separation, recirculation, reattachment and stasis. These flow disturbances lead to low and oscillating WSS and, consequently, to IH development. Recirculating flow volume is an indicator of stagnation flow region, in which long residence times of platelets and coagulation factors occur. In order to identify the recirculating flow volume, mean axial velocity has been computed as the component of the mean velocity vectors of each bulk node with respect to the direction of the centerline. Then, recirculating flow volume has been calculated as the sum of elements volume of discretized domain whereby axial velocity is negative.

Chapter 3

Results and discussion

In this chapter, results of unsteady-state numerical simulations are illustrated. At first, it has been analyzed velocity distribution at specific section of graft and venous anastomosis. Then, wall-based and bulkflow descriptors are visualized. Concerning wall-based descriptors, wall shear stress results are analyzed before in the entire AVG model and then, the attention is focused on a region of interest at the toe of venous anastomosis, the favourite site of IH. As regards instead bulk-flow, helicity-based descriptors has been computed. In conclusion, recirculating flow volume has been calculated in order to localize and quantify recirculation zone, which lead to flow separation areas.

3.1 Velocity

In Figures 3.1- 3.3, the velocity magnitude and in-plane streamlines of two cross-sections are visualized at three different time instants of cardiac cycle: at early systole (0.090 s), peak systole (0.185 s) and late systole (0.340 s). The cross-section A is at venous anastomosis and B is 10 mm downstream of section A, in the draining vein.

At early systole (Figure 3.1), maximum velocity distribution at section A of the all models is located at half high section. At this time instant of cardiac cycle, it is possible to observe that velocity distribution of AVG LFD-1 is very similar to reference Base model and velocity of AVG HFD-1 is similar to Helical model, except for the direction of rotation of the flow. This means that this flow divider positioning does not particularly influence the hemodynamics at venous anastomosis and in the draining vein. Instead, concerning section A of LFD-2, LFD-3 and HFD-2 models, as flow divider ends close to venous anastomosis, it is possible to visualize three regions of high velocity corresponding to the three separated flows deriving from flow divider channels. This can not be viewed at section A of HFD-3, because the flow undergoes a greater mixing within flow divider. Instead, by its streamlines, it is possible to notice a great vortex with its center close to anastomosis wall. Regarding the velocity observed in section B, AVGs with linear flow divider, have a flow symmetry with the development of two central counter-rotating vortices, and two secondary vortices are present at right and left sides of venous wall. Section B of AVGs HFD-1 and HFD-2 shows a main vortex and a secondary one at left side of venous wall. Fluid domain of the latter models have a direction of rotation opposite to that of the Helical model because forward direction of helical flow separator is not concordant with that of reference AVG Helical. Section B of HFD-3 model only presents a single great vortex.

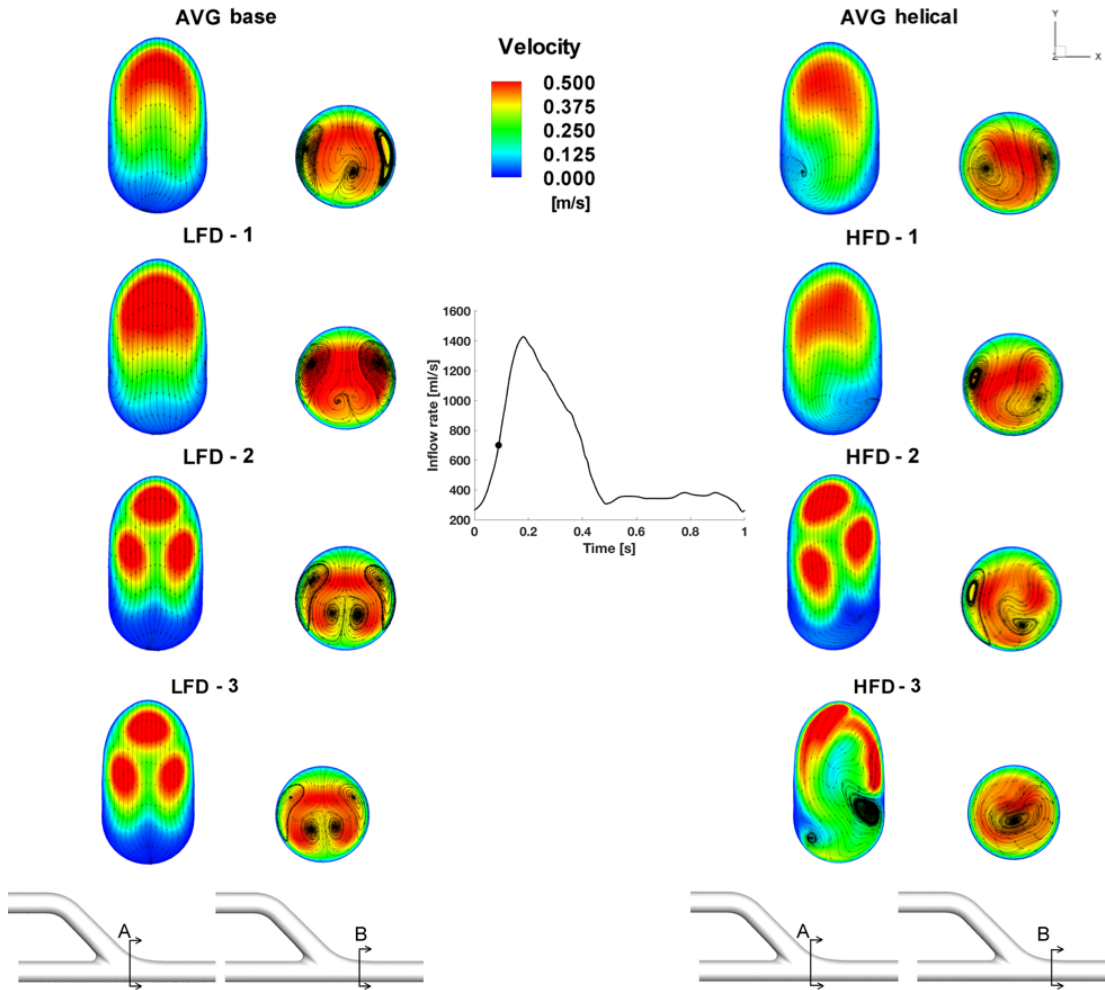


Figure 3.1: Velocity magnitude contours and in-plane streamlines at early systole (0.090 s) for two different cross section: at venous anastomosis (section A) and 10 mm downstream of that (section B).

Velocity distributions at peak and late systole instants are characterized by similar features (Figures 3.2, 3.3). In detail, section A shows flow recirculating zones near the venous floor. Concerning section B, in LFD-1 configuration, it is observed a typical Dean flow, with two counter-rotating flow structures. The flow inside AVG HFD-3 is confirmed to be of considerable interest, thanks to the only vortex in which all fluid domain is involved throughout the cardiac cycle. To better understand hemodynamics inside flow divider, tangential velocity vectors of section C are visualized in Figure 3.4. Cross-section C is taken at 10 mm upstream of curved venous segment of venous graft. At this section, all of LFD

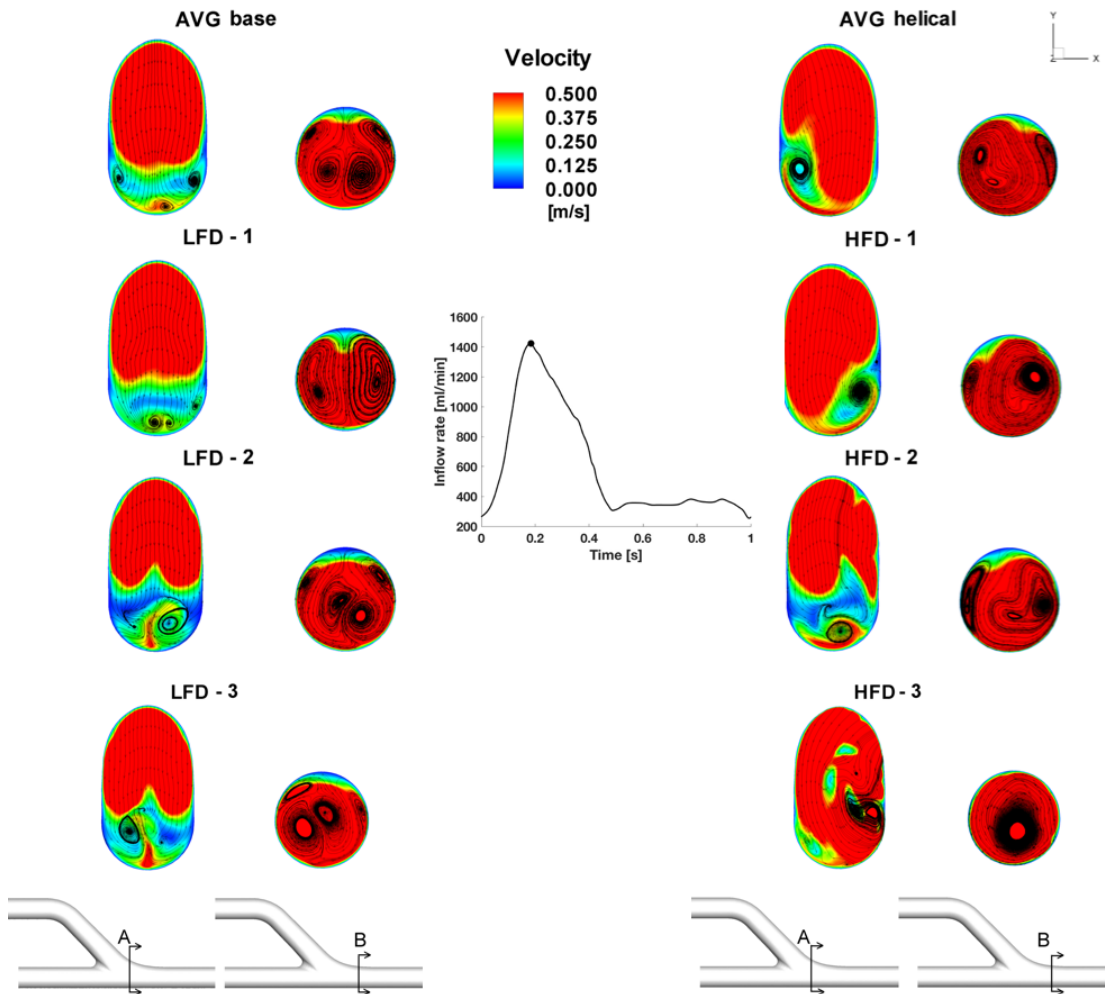


Figure 3.2: Velocity magnitude contours and in-plane streamlines at peak systole (0.185 s).

and HFD models have flow divider. From velocity vectors, it can be seen that blood, which flows inside HFD models, is involved in a unidirectional flow. Contrariwise, in LFD models the flow separated in three regions has a peak of velocity at the center of each flow divider section and at their extremities secondary vortices can be generated. In Figure 3.5, time-averaged velocity magnitude distributions can be visualized, for a cross-section along the x-direction at half of the venous diameter. This representation is useful to understand flow behaviour at the venous insertion of the modeled vascular accesses. The branching at venous anastomosis is a source of disturbed flow and causes variation in the mean velocity. For the first two novel model designs, LFD-1 and HFD-1, in which flow

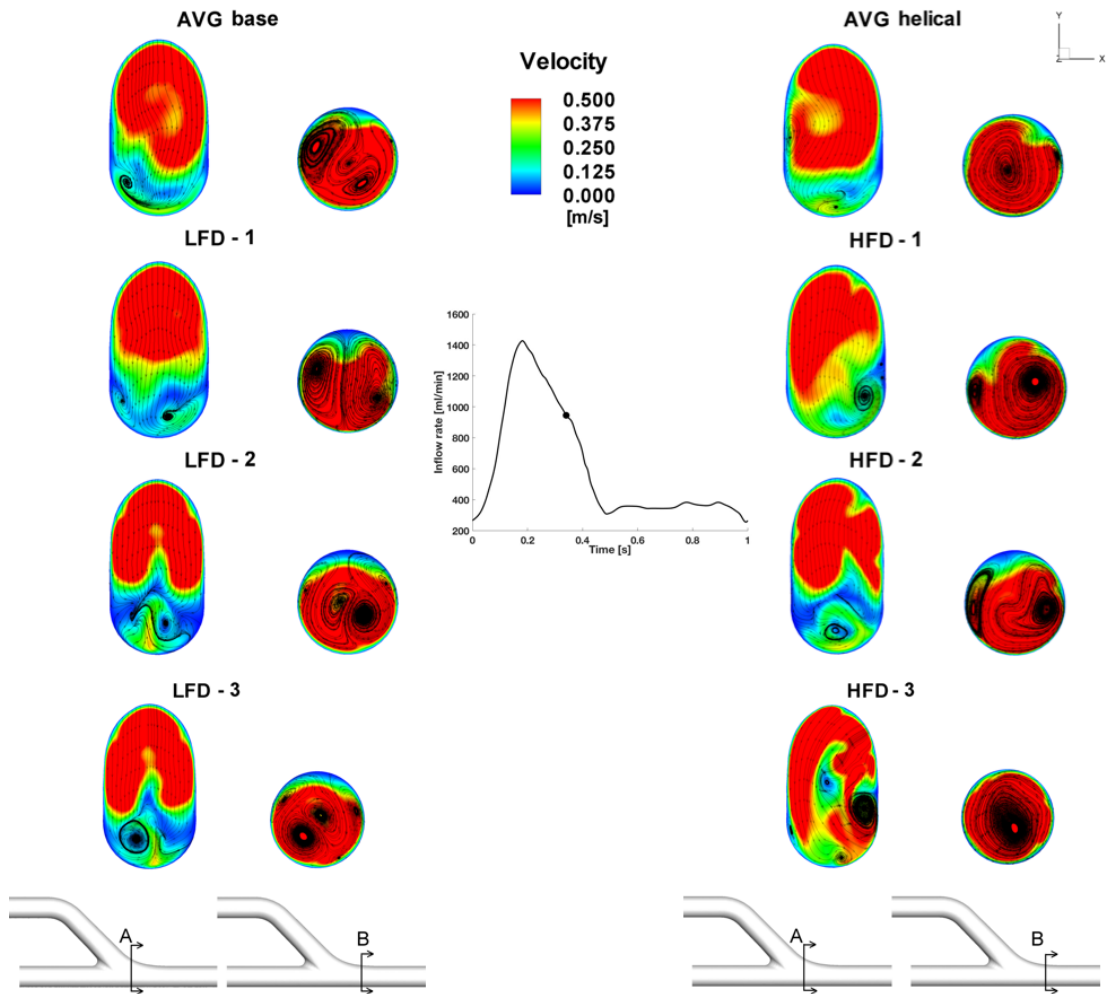


Figure 3.3: Velocity magnitude contours and in-plane streamlines at late systole (0.340 s).

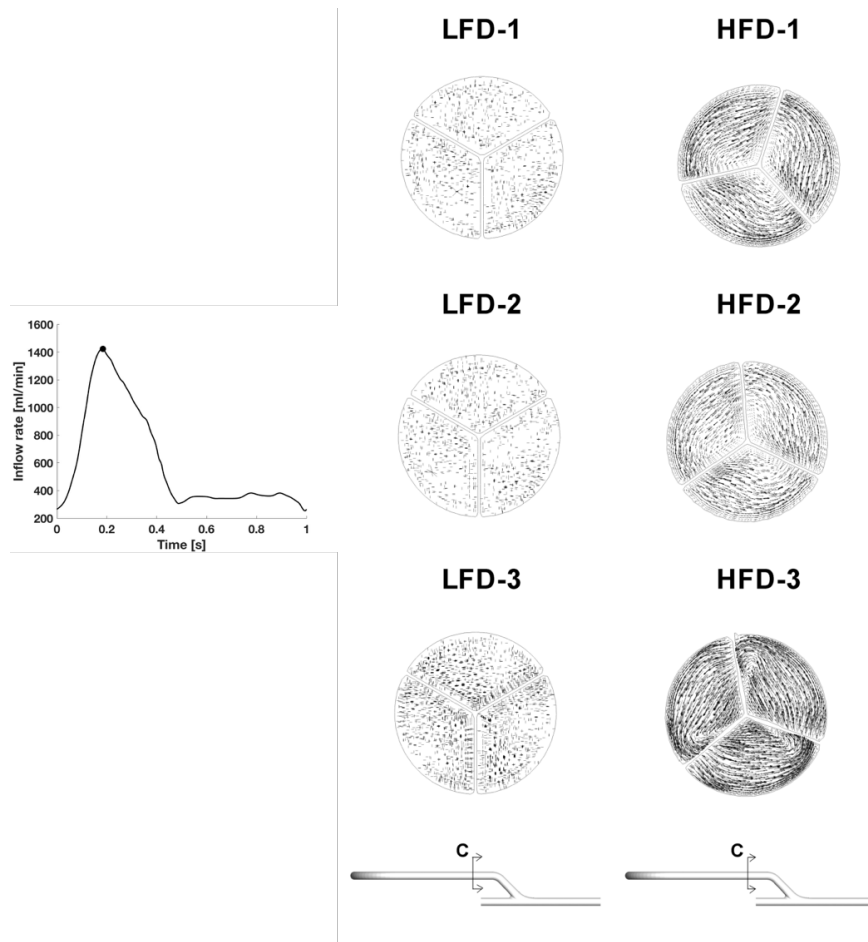


Figure 3.4: Velocity vectors at a cross-section of flow divider.

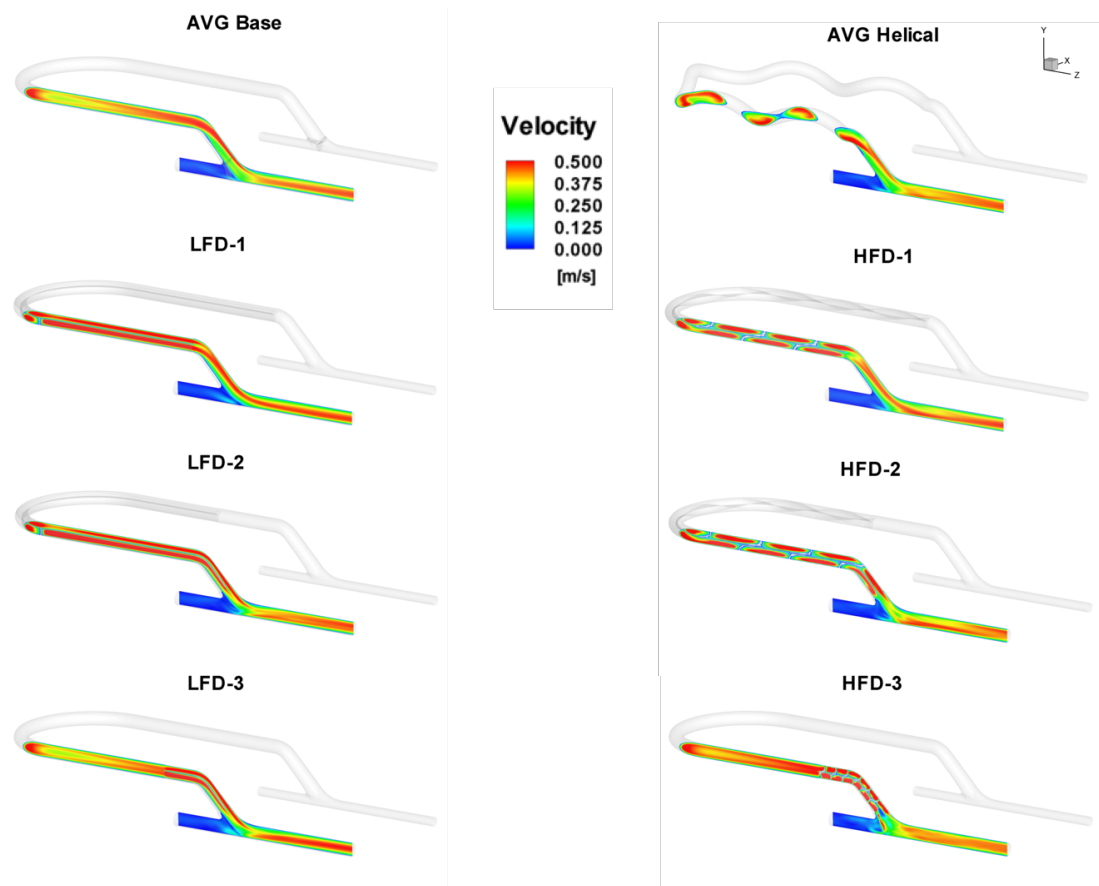


Figure 3.5: Time-averaged velocity contour levels of a cross-section along x direction.

divider doesn't end close to venous anastomosis, in the 45° inclined segment of the graft high velocity flow is shifted to upper part of graft wall. In proximal venous segment, near the upper wall of the vein a region of low velocity is generated. This region is not visible in HFD-3 model, in which the blood flow quickly becomes developed, but its velocity distribution is more complex at the exit of flow divider.

3.2 WSS-based descriptors

Many researchers supported the theory according to which IH develops mostly in regions with near-wall hemodynamics exhibits low TAWSS, high OSI and high RRT. In Figure 3.6, TAWSS contour levels of a zoomed venous anastomosis and draining vein areas are illustrated. According to this, low TAWSS areas are visualized at the anastomosis region of all models, except for the model HFD-3. As observed at the venous floor area, for HFD-3 model, low TAWSS area is marginal to distal vein segment, while for linear and the other helical models, this low shear stress region is extended to surface close to anastomosis.

In order to have an explicit representation of pro-atherogenic areas, TAWSS values at the entire luminal surface of the all models are clustered and two threshold values equal to 10th and 20th percentiles have been calculated and visualized in Figure 3.9. As observed in base and helical AVGs, low TAWSS are at luminal surface where the blood flow has a change in direction, in particular in the intrados of looped tract, because the peak of velocity profile is shifted towards the extrados of the curve. This is also detectable in LFD-3 and HFD-3 models, in which flow divider is at the end portion only of the graft. In regions with flow divider, low wall shear stress areas are present on rounded edges of each section of flow divider. At the exit of the latter, small region of low TAWSS is encountered, because of the flow passes from a section with a smaller diameter to a section with a larger diameter, thus secondary flows at these points are generated. Percentile values representations confirm which are visible in contour plots, that is, the venous anastomosis and the draining vein surface areas of HFD-3 model only are not exposed to low WSS.

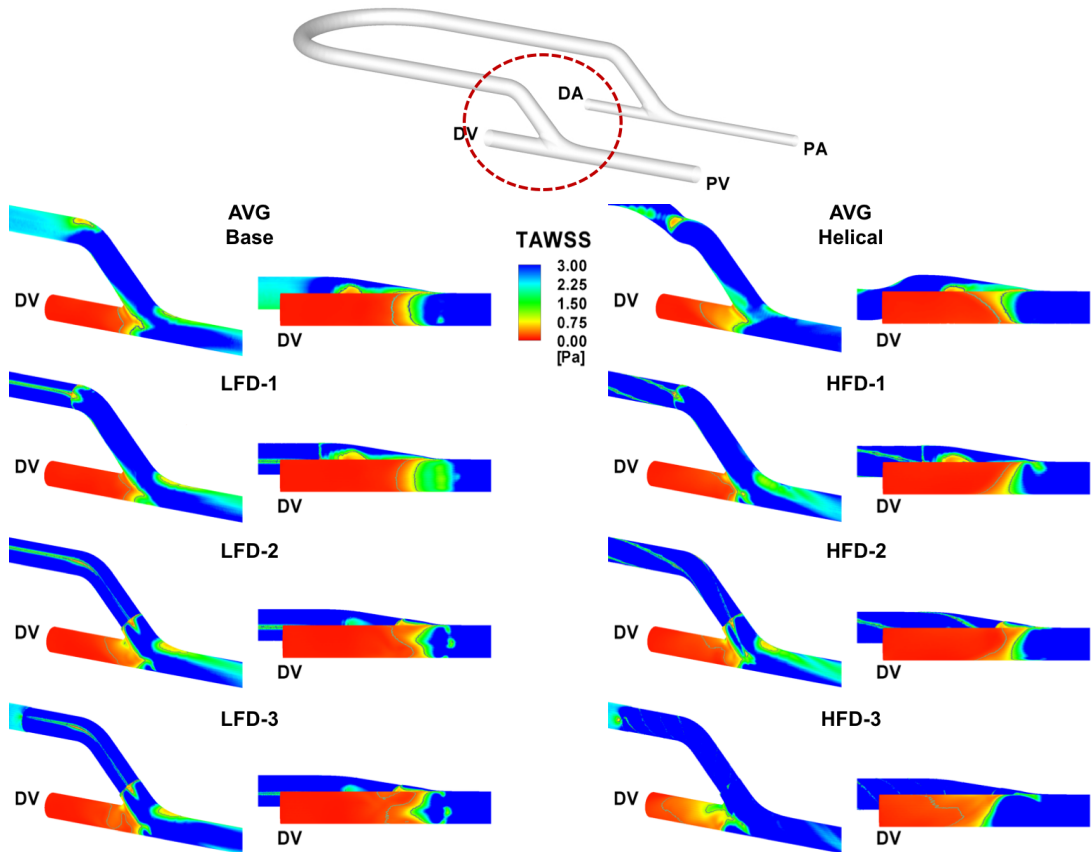


Figure 3.6: Zoom representation of TAWSS contours of venous anastomosis area.

Concerning OSI distributions, in Figure 3.7 it is possible to see that OSI values are very low (below 0.1) in most of the surface wall, meaning that the WSS vectors do not present significant directional changes over the cardiac cycle. Therefore, the descriptor OSI is not very explicative, and 80th and 90th percentile values, visualized in Figure 3.7, are not demonstrative of high OSI exposed areas. As seen in Figures 3.8 and 3.11, RRT contour levels follows strongly TAWSS contours. This is clearly visible in percentile values contours (Figures 3.9 - 3.11), in which TAWSS20th-10th and RRT80th-90th are localized in the same areas for each luminal surface model.

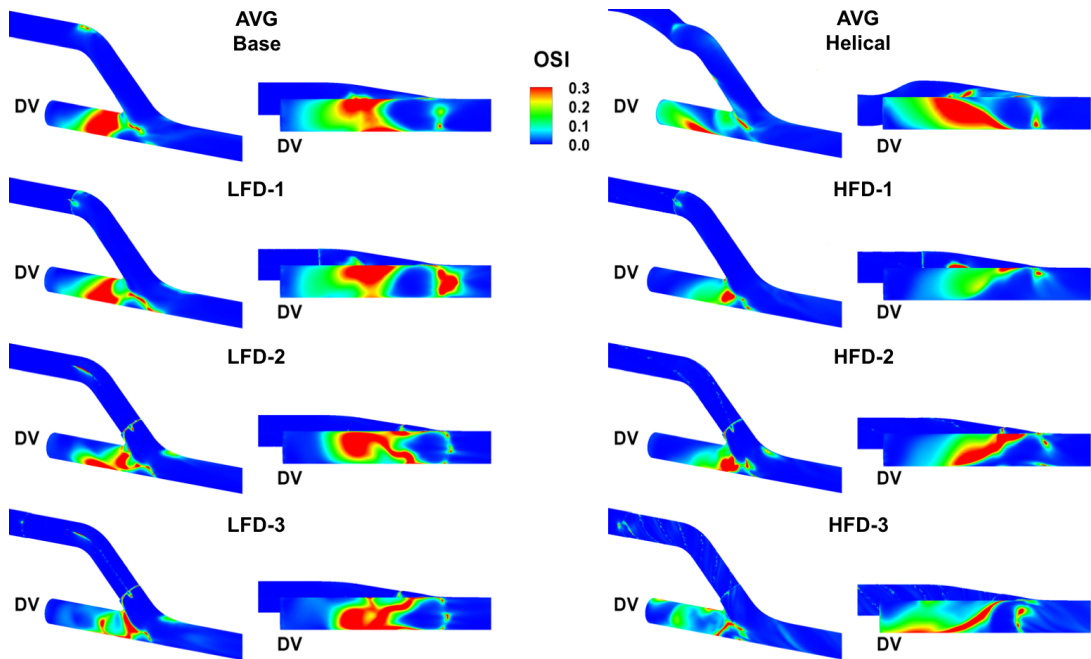


Figure 3.7: Zoom representation of OSI contours of venous anastomosis area.

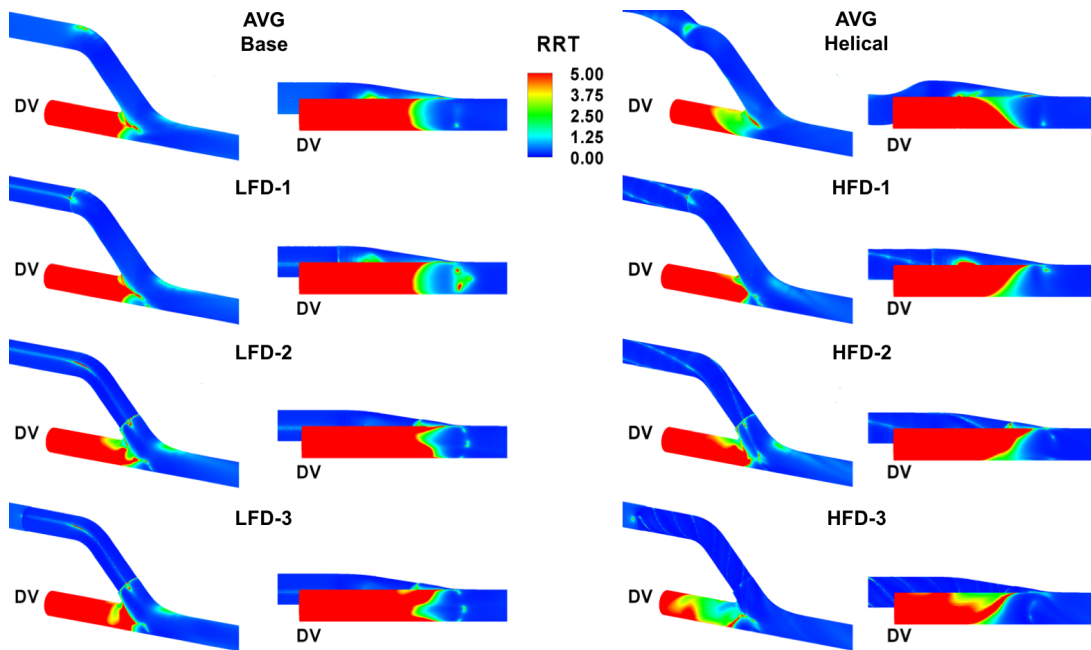


Figure 3.8: Zoom representation of RRT contours of venous anastomosis area.

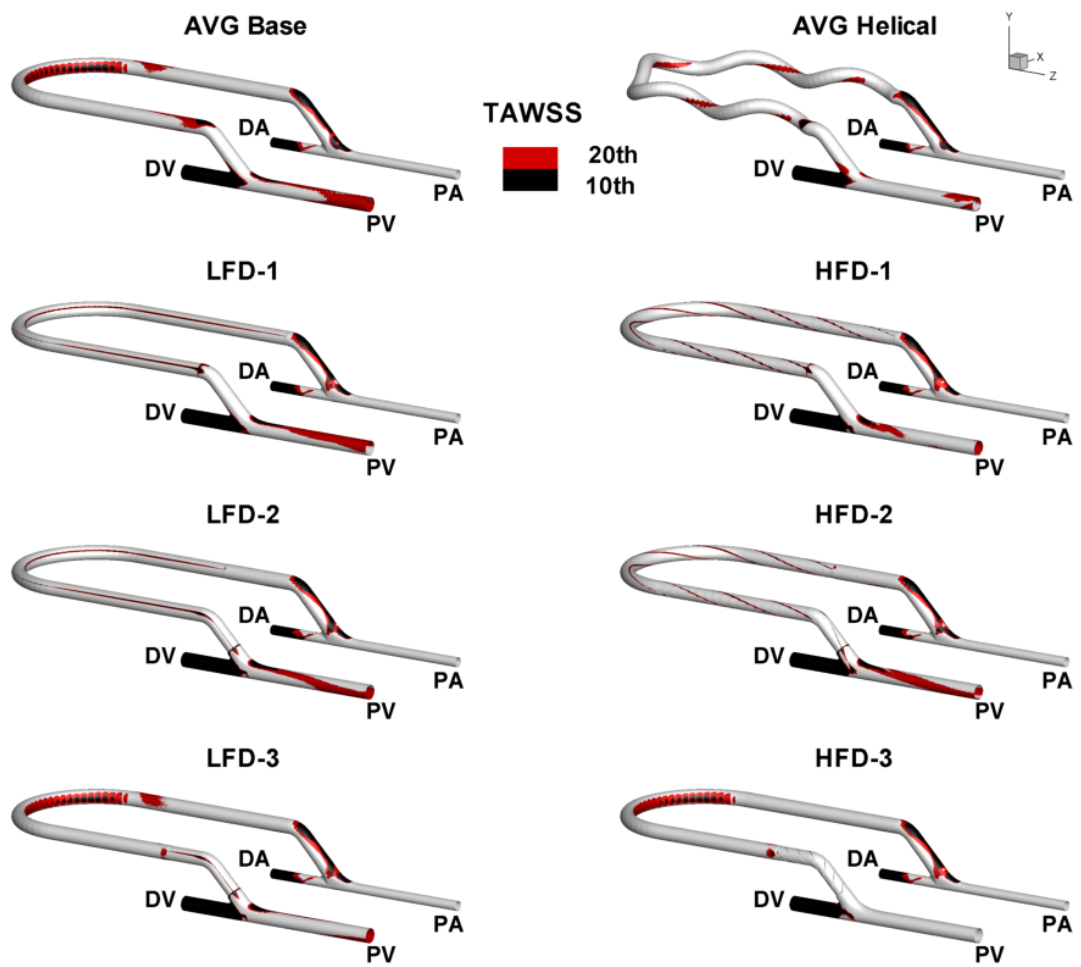


Figure 3.9: Contour levels corresponding to 20th and 10th percentile TAWSS values.

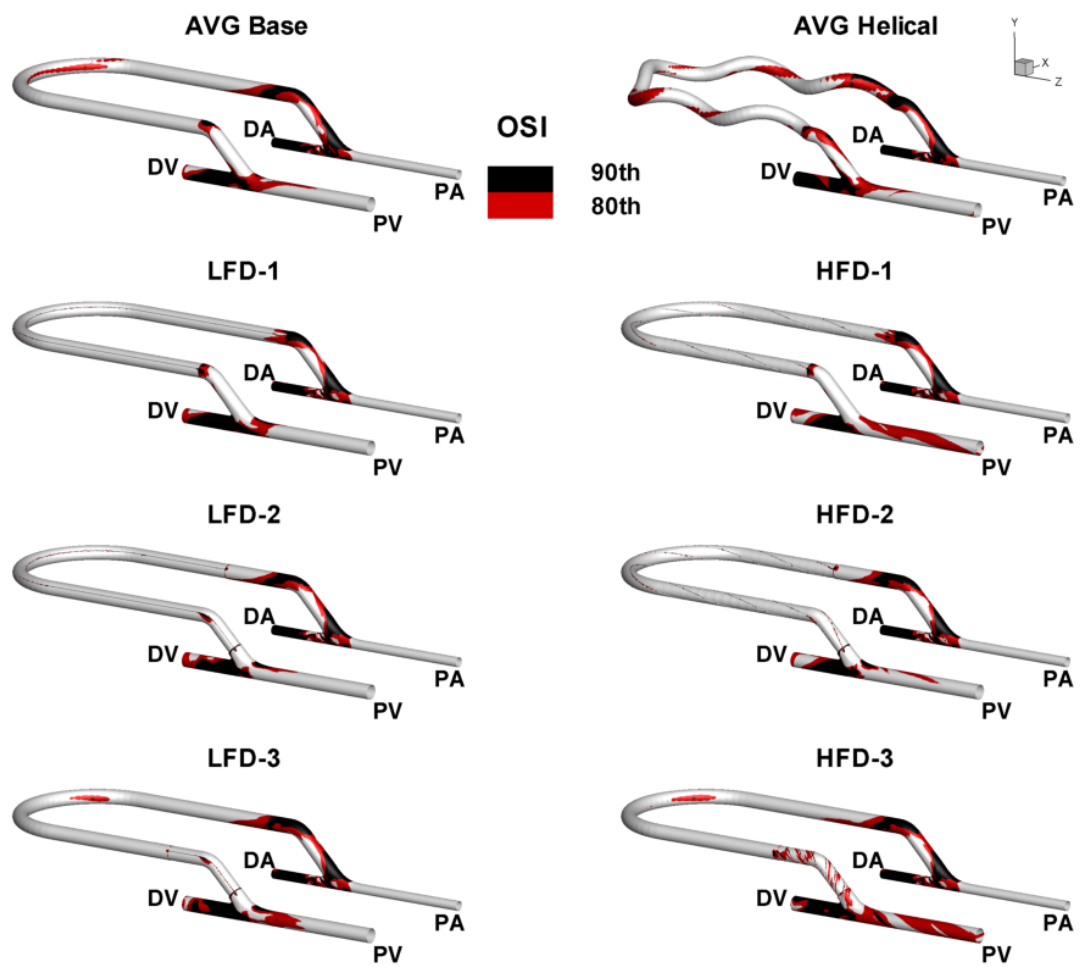


Figure 3.10: Contour levels corresponding to 80th and 90th percentile OSI values.

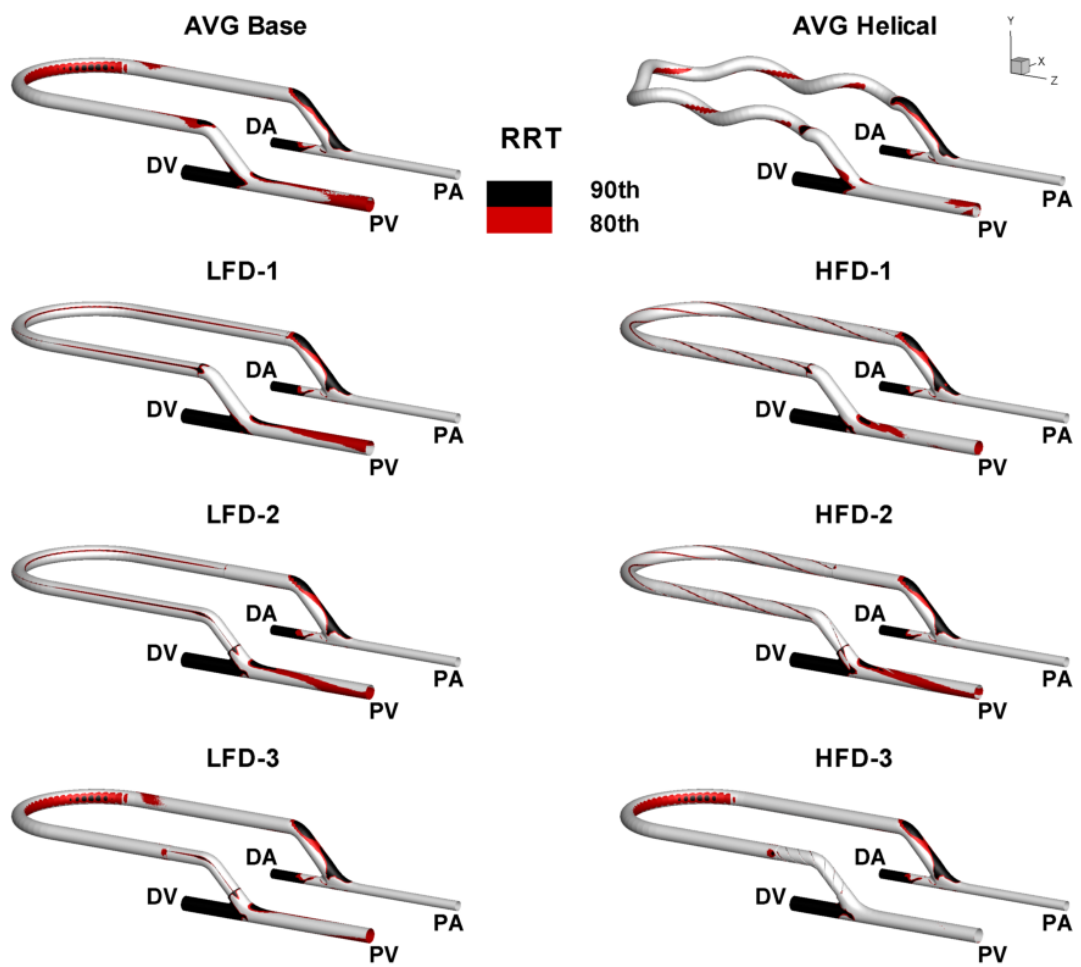


Figure 3.11: Contour levels corresponding to 80th and 90th percentile RRT values.

3.2.1 WSS-based descriptors in region of interest

To quantify and localize potential disturbed shear areas at venous anastomosis, a region of interest (ROI) has been selected in Matlab (Figure 3.12). At this ROI, WSS-based percentile values of WSS-based descriptors are calculated. Percentile values of TAWSS, OSI and RRT have been reported in Table 3.1. It is worth to note that percentiles values of TAWSS are very high and OSI percentile values very low. In Figure 3.13, contour levels of TAWSS are visualized, focusing on the selected ROI.

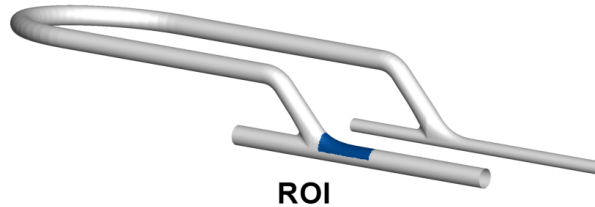


Figure 3.12: Visualization of ROI.

Table 3.1: Percentile values of WSS-based descriptors in ROI-1 and ROI-2.

Percentile values	
TAWSS 20th	1.6565 Pa
TAWSS 10th	1.2555 Pa
OSI 80th	0.0164
OSI 90th	0.0259
RRT 80th	0.6157 Pa ⁻¹
RRT 90th	0.8284 Pa ⁻¹

As observed in Figure 3.13, Base and LFD models have a large area subjected to low TAWSS. The amount of surface area exposed to TAWSS below (OSI and RRT above) percentile values are reported in Table 3.2. To confirm what has been seen in TAWSS contour plots, surface area of HFD-3 exposed to low shear stress is exactly null. Concerning the other AVGs HFD, surface areas exposed to

low shear stress of HFD-2 is slightly larger than that of HFD-1. As regards LFD AVGs, luminal surface area involved in low WSS are approximatively equivalent, but it results larger than AVG Base. About LFD models, mean TAWSS is lightly smaller than AVG base. From Table 3.2, it is also possible to note that surface area exposed to high RRT is equivalent to surface area exposed to low TAWSS, and, according to Figures 3.17 - 3.18, it can be state that these surface areas are co-localized.

Then, to better analyze found results, statistical approach is used. More in detail, averaged values and standard deviations of TAWSS, OSI and RRT in ROI has been calculated for each model. Bar chart of TAWSS (Figure 3.20) shows that mean TAWSS of HFD-3 is about 50% higher than mean TAWSS value of other models. Moreover, it presents the smaller standard deviation. Bar chart of OSI mean explicates that mean value is in the range of $0.01 \div 0.02$, that is very low. For AVGs LFD-1, LFD-2, HFD-2 and LFD-3, OSI standard deviation was higher than its mean value. Therefore, it has been plotted histograms of their OSI distribution (Figure 3.19) and discovered that, for these models, maximum of OSI values range is extended to 0.25, while for the other models the OSI values are in the range $0 \div 0.05$. About these models, standard deviation errorbar for OSI below mean value level produces an incorrect information, because OSI values can not be negative. Therefore, below OSI mean value level errorbar rapresents the minimum OSI value. As observed in these bar charts, LFD-2 and LFD-3 have the worst behaviour. Among HFDs, high mean OSI value is found for HFD-2, which is higher than reference Helical model.

In conclusion, percentage variations of mean WSS-descriptors values respect to conventional straight AVG have been computed. The first bar chart (Figure 3.21) revealed that mean values TAWSS of HFD-3 is about 40% greater than mean TAWSS of Base model, compared to less than 5%, that is the percentage variation of mean TAWSS of reference Helical model. As regards OSI mean, AVG HFD-3 presents a percentage variation of -1% and it is the only model with a negative difference. Mean OSI values of the above mentioned models are about 0.01. Making a further comparison with Helical model, it was found that OSI percentage difference of this model respect to Base model is about 60%. About

RRT values, it is noticed that models with a negative percentage variation are AVGs Helical, HFD-1 and HFD-3. Among these, HFD-3 presents the highest difference (about -40%), compared with -14% of RRT mean value of Helical model. Moreover, observing bar charts of TAWSS and RRT mean values, it is possible to confirm that RRT values are intrinsically related, except for the sign, to TAWSS values. According to these charts, HFD-3 model results more efficient than Helical model in preventing intimal hyperplasia which affects venous anastomosis.

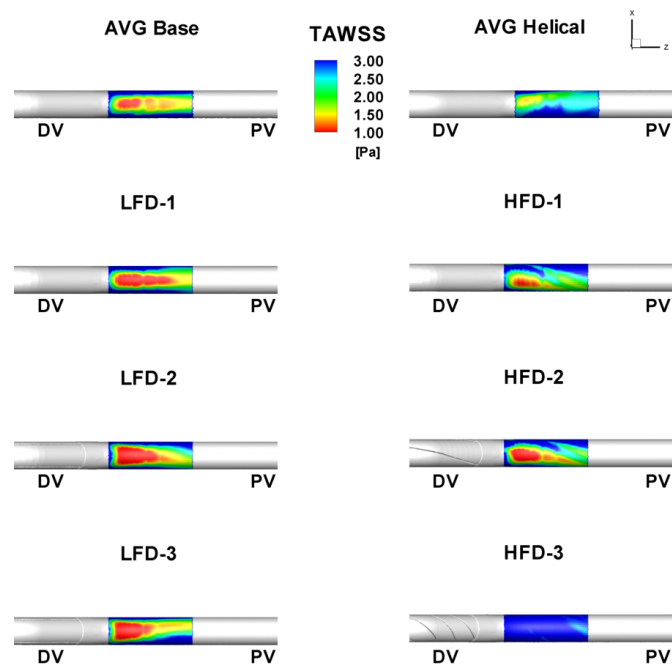


Figure 3.13: Contour levels of TAWSS in region of interest.

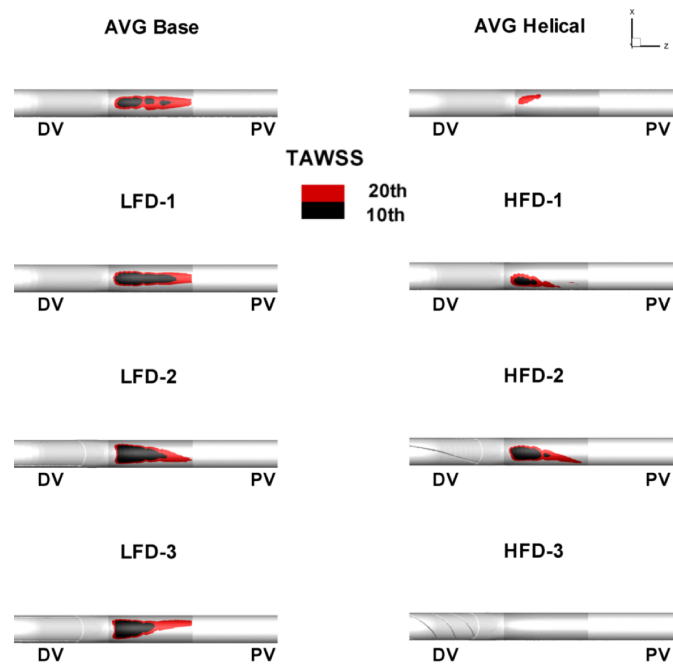


Figure 3.14: TAWSS percentile values levels in ROI.

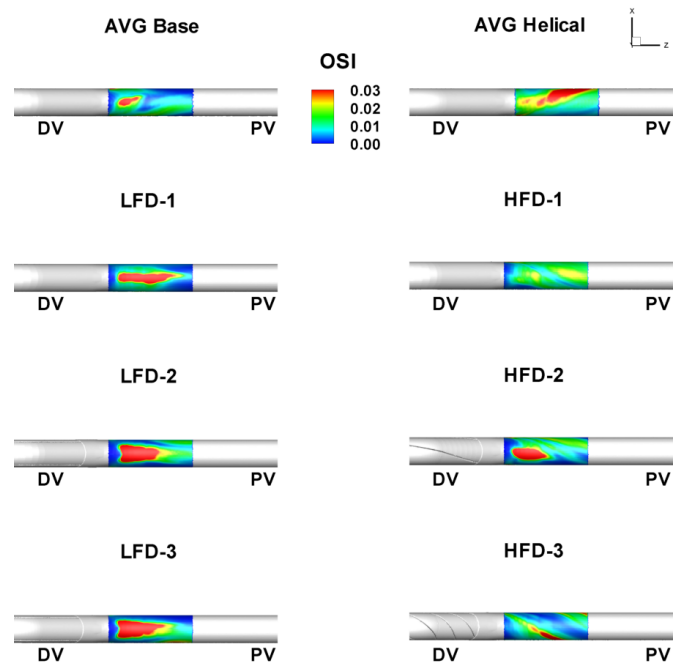


Figure 3.15: OSI contour levels in region of interest.

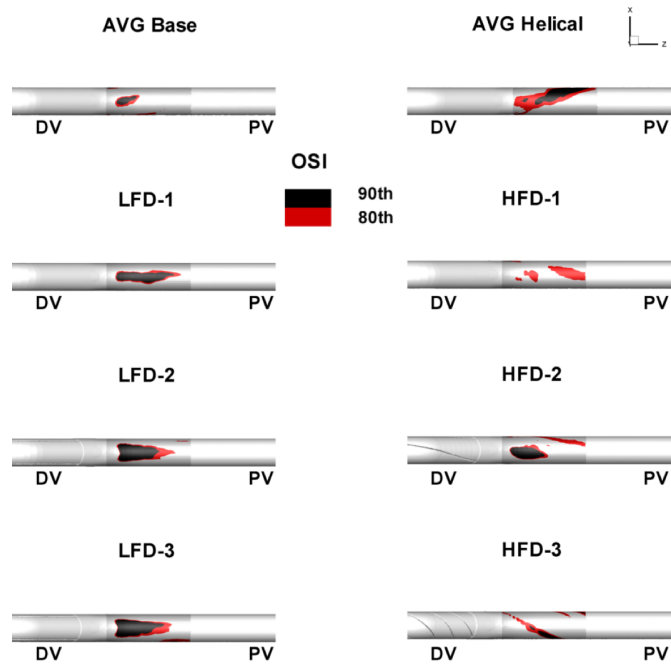


Figure 3.16: OSI percentile values levels in ROI.

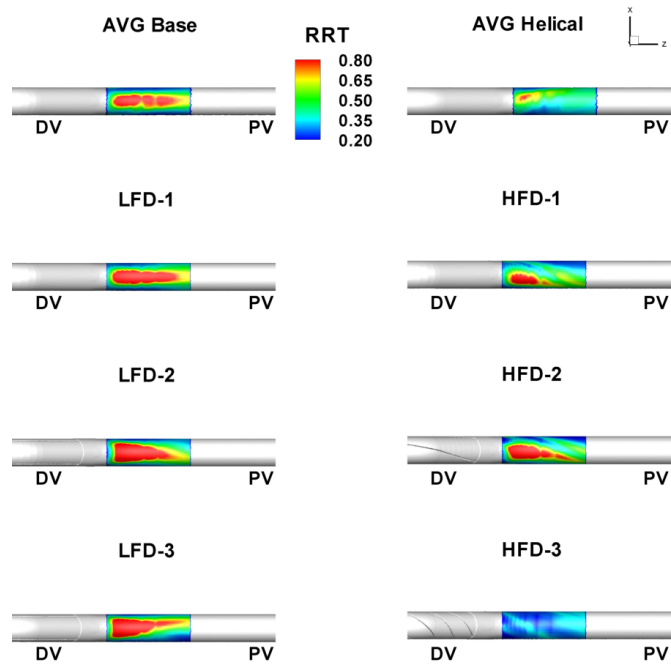


Figure 3.17: RRT contour levels in region of interest.

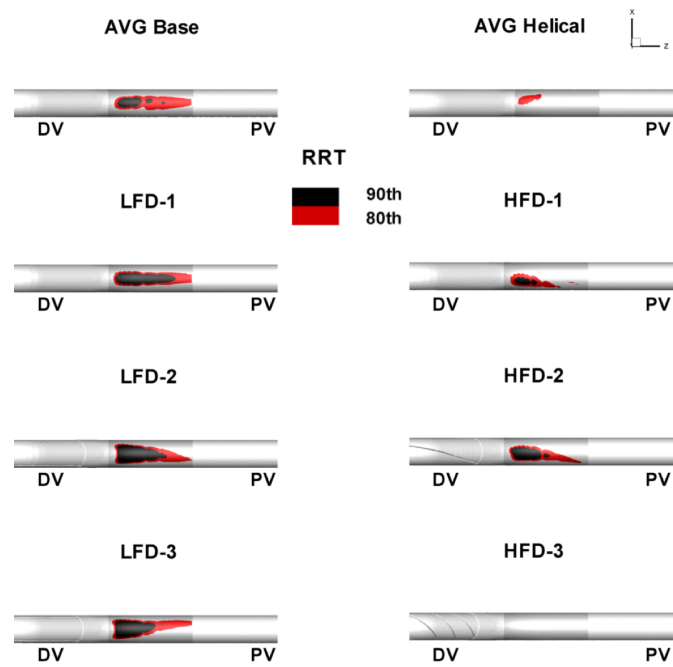


Figure 3.18: RRT percentile values levels in ROI.

Table 3.2: ROI surface area exposed to low TAWSS, high OSI and high RRT.

Models	Area [mm ²]					
	TAWSS 20th	TAWSS 10th	OSI 80th	OSI 90th	RRT 80th	RRT 90th
Base	21.7	7.0	12.9	4.0	21.9	5.6
Helical	3.6	0	32.7	14.8	4.1	0
LFD-1	24.2	13.8	14.9	10.2	24.0	13.6
HFD-1	11.8	3.8	13.6	1.4	12.1	3.6
LFD-2	27.0	15.9	19.9	13.5	27.0	27.4
HFD-2	19.4	8.9	21.0	9.9	19.7	9.4
LFD-3	26.0	13.2	26.0	14.8	25.8	13.7
HFD-3	0	0	13.7	4.7	0	0

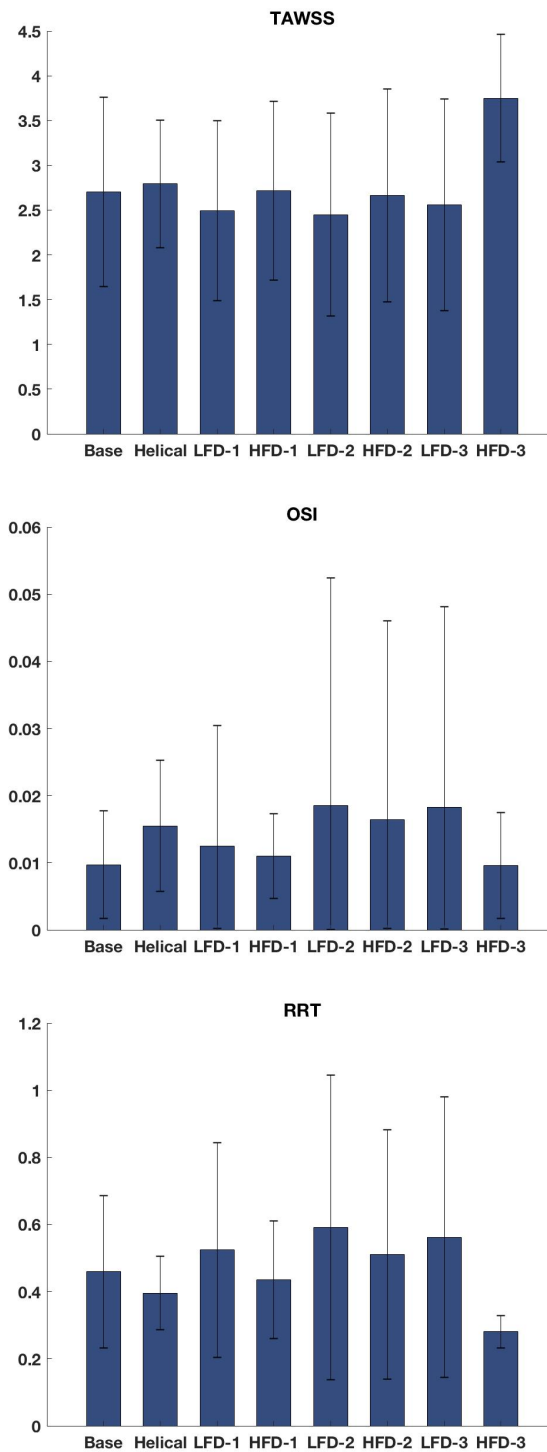


Figure 3.20: WSS-based descriptors mean values and standard deviations.

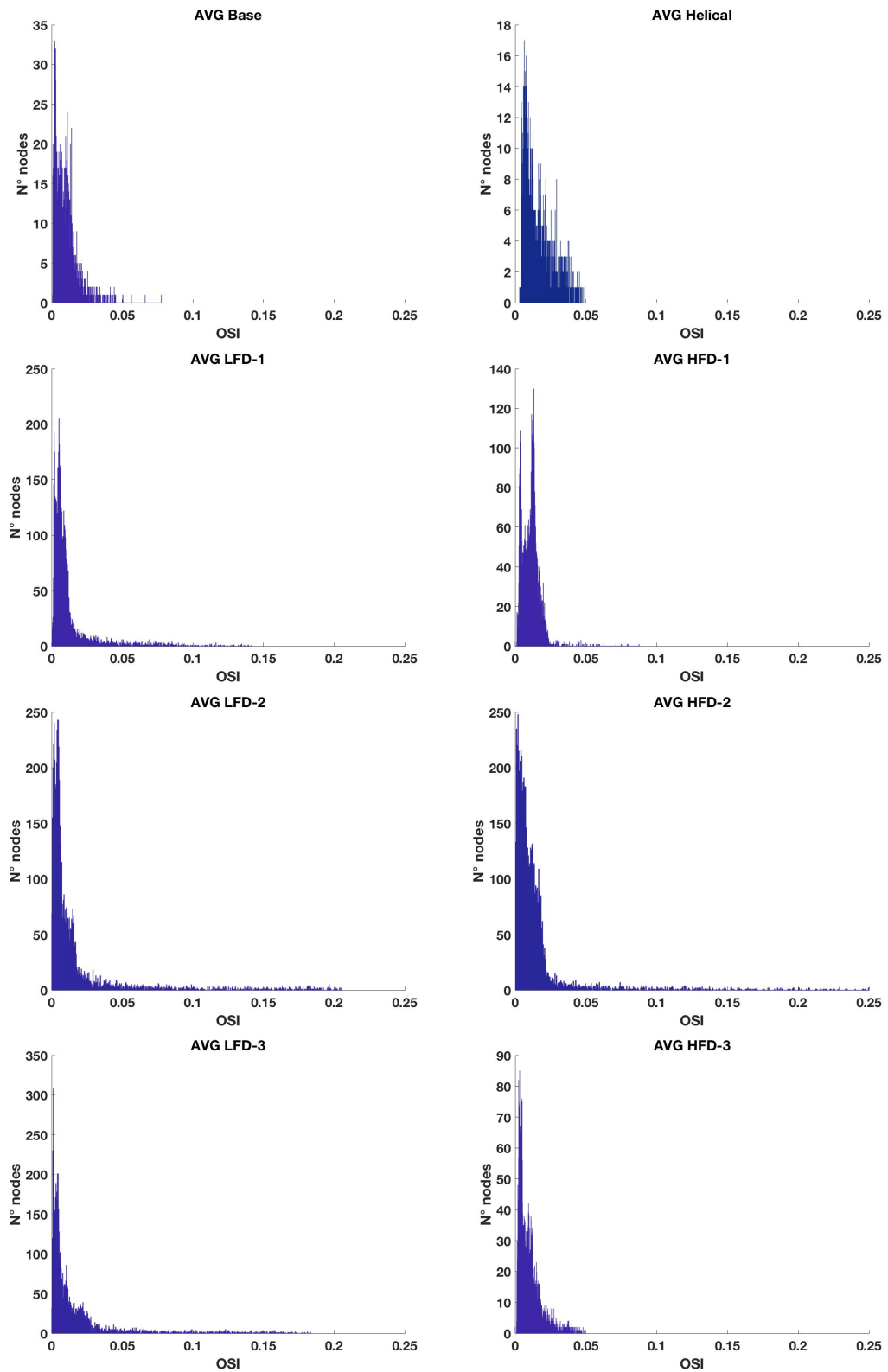


Figure 3.19: Histograms of OSI values distribution in region of interest.

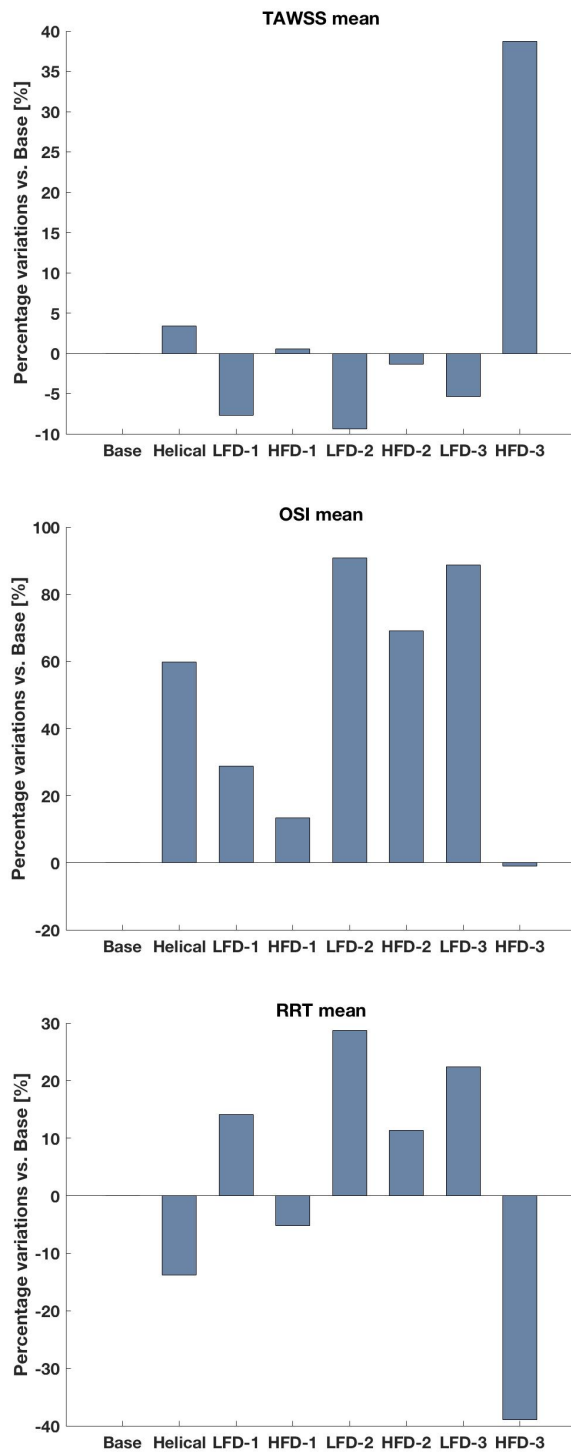


Figure 3.21: Percentage variations vs. Base of WSS-based descriptors mean values.

3.3 Helicity-based descriptors

To visualize counter-rotating structures in the bulk flow, LNH descriptor is used, that gives an idea of the alignment or disalignment of velocity and vorticity vectors. It has been chosen two threshold values, ± 0.4 and ± 0.7 .

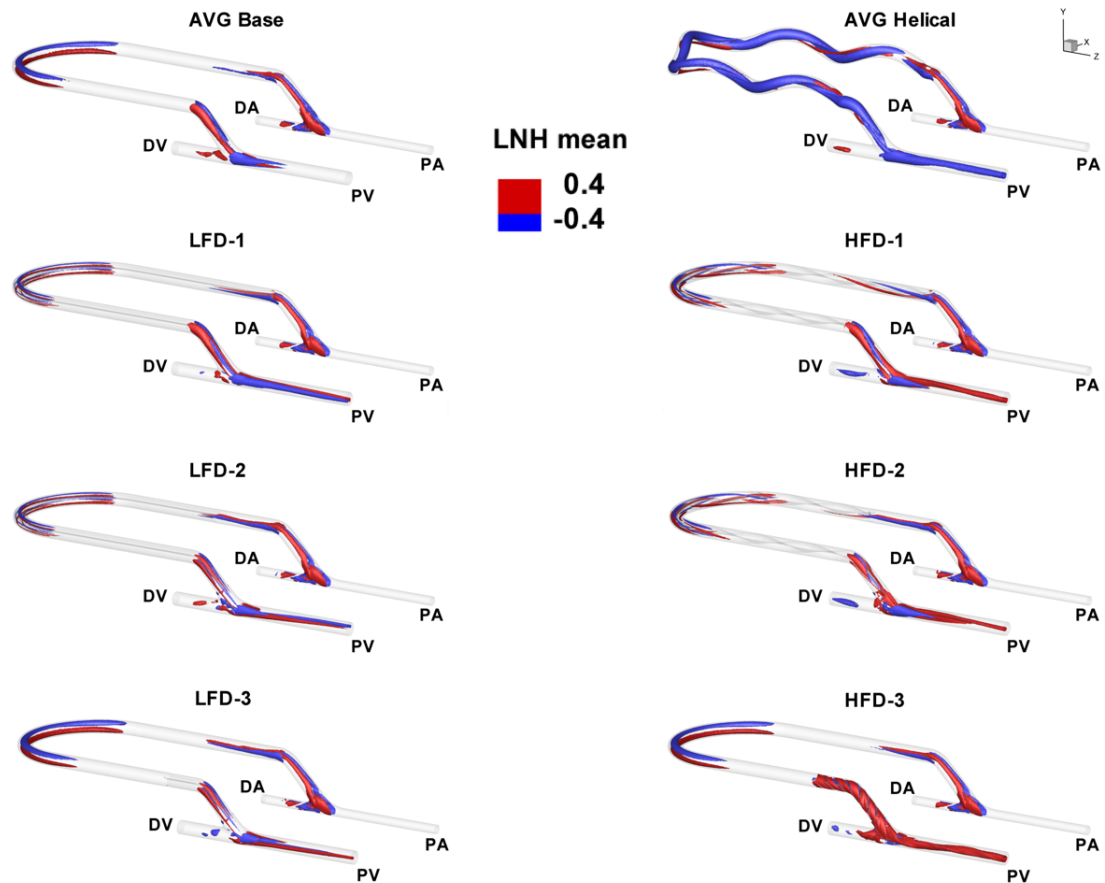


Figure 3.22: Iso-surfaces of time-averaged LNH for the eight simulated models, adopting a threshold value equal to ± 0.4 .

In Figure 3.22, iso-surfaces corresponding to time averaged $\text{LNH} = \pm 0.4$ are displayed. It is immediate to observe that helical flow structures originate in close proximity to curvatures, in particular at arterial anastomosis, at looped part of the graft and at its outlet part. They are also kept for the whole length of proximal vein, except for Base model. It is possible to see symmetrical counter-rotating structures (positive values of LNH characterize right-handed helical structures, while negative values indicate those left-handed), in which the centerline of con-

duit is the center of symmetry. It is also adopted an high threshold value of LNH (± 0.7) to visualize helical flow patterns. Adopting a LNH threshold value close to 1, it's possible to visualize an almost purely helical flow.

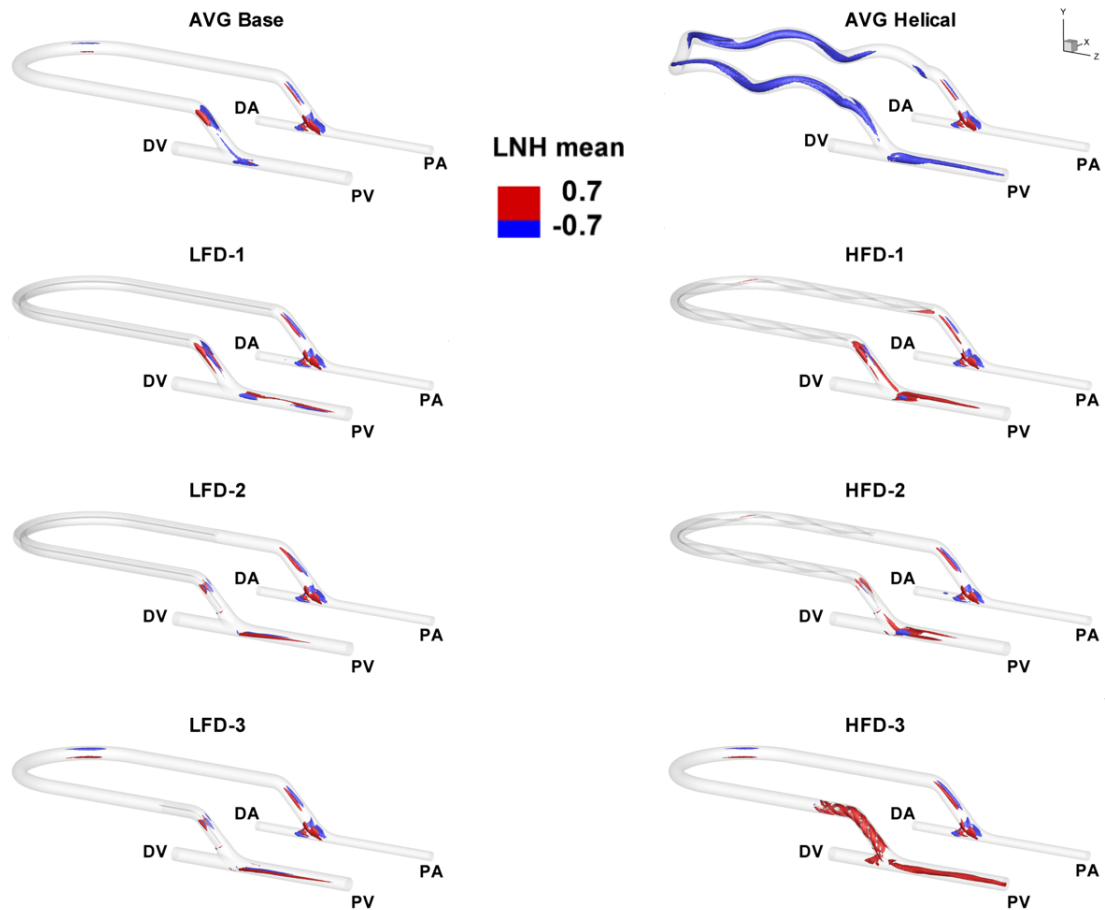


Figure 3.23: Iso-surfaces of time-averaged LNH for the eight simulated models, adopting a threshold value equal to ± 0.7 .

Iso-surfaces of time-averaged LNH equal to ± 0.7 are shown in Figure 3.23. It can be said that, approximatively, almost all of the models have a limited volume at anastomotic zones, in which the flow is considered purely helical. This is not true for Helical model, in which counter-clockwise helical structures is also found in looped section of the graft and downstream of venous anastomosis. Interesting flow patterns are also visualized in HFD-3 model, in which a clockwise helical flow structure is visible at each channel of flow divider and it is preserved in proximal

vein. This fluid pattern enforces the single vortex visualized in streamlines of velocity contour plots. The clockwise or anticlockwise rotation of blood flow in the last two mentioned models is due to the direction of helix rotation.

In Figure 3.24, LNH iso-surfaces (± 0.7) at peak-systolic time instant are visualized. For AVG HFD-3, a very intertwined counter-rotating structure is visible inside flow divider and at proximal vein. Inside of the other HFD models, intertwined helical structures at proximal vein are not visible, but counter-rotating helical structures remain separated. The smaller helical pitch of flow divider is the key factor of particular structures observed in HFD-3 model.

To quantify intravascular structures, quantitative helicity-based descriptors are computed for the all simulated models, which are represented by bar charts (Figure 3.25). Descriptor h_1 , that is the time averaged helicity value normalized respect to the volume, presents a negative value for the models taken as reference. This means that left-handed helical structures characterize bulk flow. For LFD models, h_1 is about 0, indicating the presence of reflectional symmetry in bulk flow, while for HFD models the predominant direction of rotation is right-handed. In bar chart related to h_2 , it is possible to see that HFD-3 model, together with Helical model, has the greater helicity intensity in fluid domain. Furthermore, HFD models presents a greater helicity than LFD ones. Descriptor h_3 shows, in percentage terms, the predominant helical structures. For HFD-3, the percentage of predominant flow structures is about 30%, concurring with Helical AVG, but they are right-handed and left-handed, respectively.

Descriptor h_4 is the absolute value of h_3 ; indeed, it give the same information of this latter, neglecting its direction of rotation.

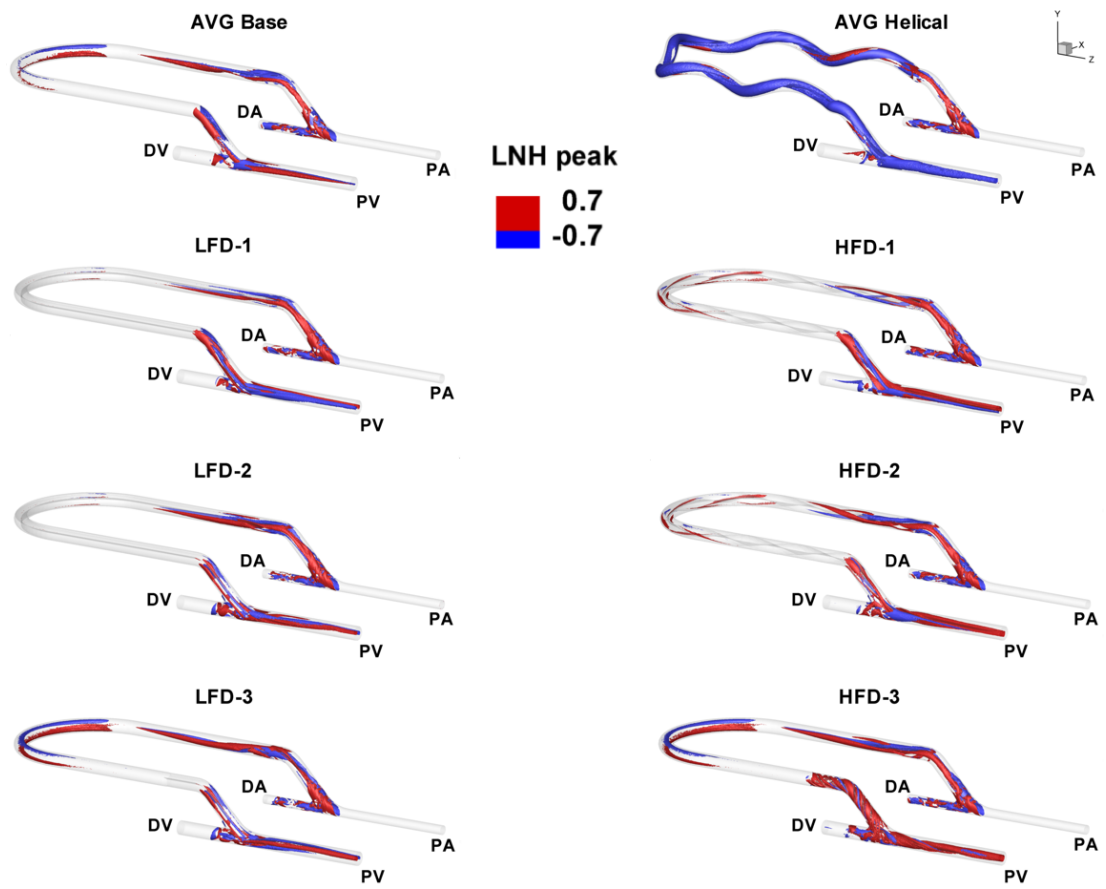


Figure 3.24: Iso-surfaces of LNH at peak systolic time instant, adopting a threshold value equal to ± 0.7 .

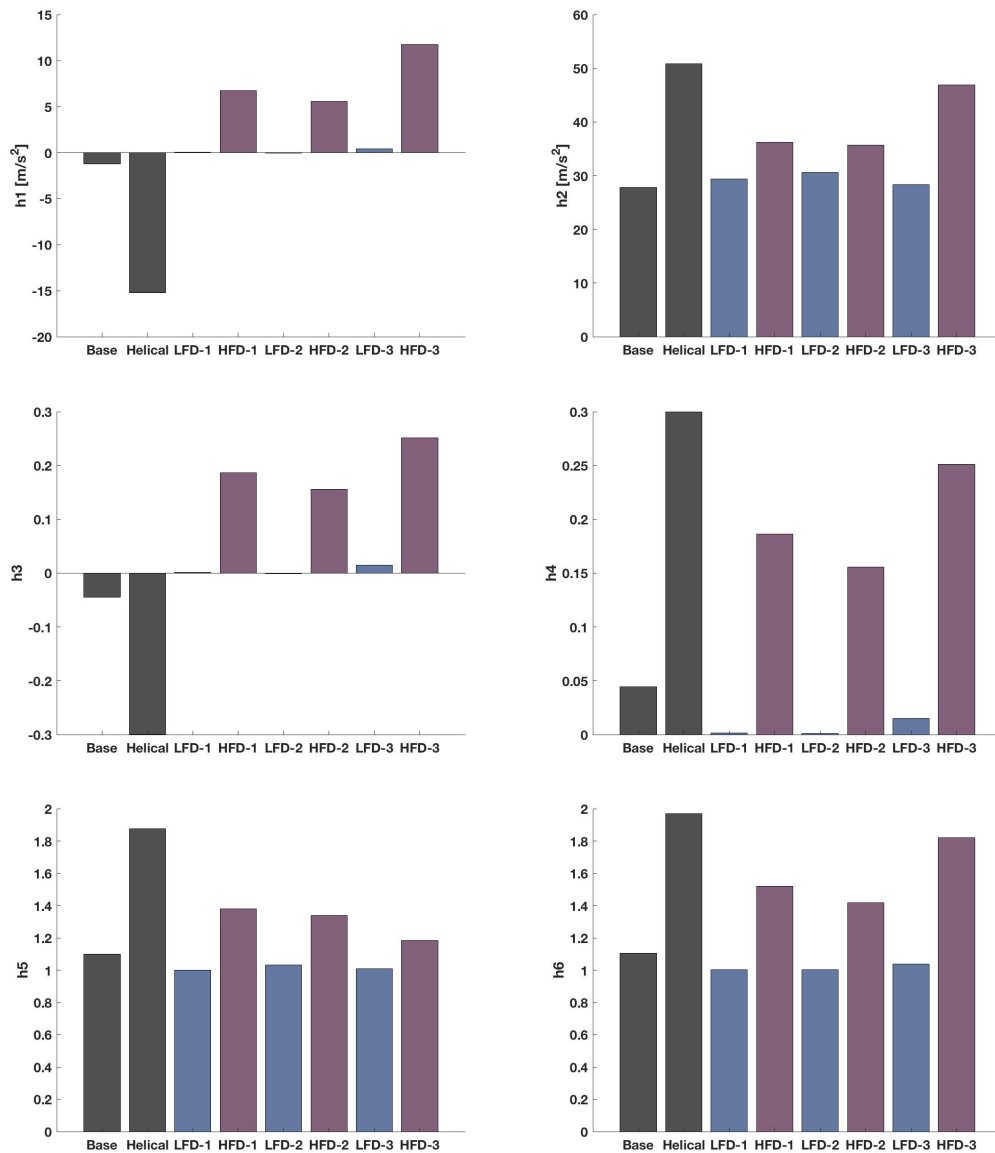


Figure 3.25: Quantitative helicity descriptors.

3.4 Recirculating flow volume

In Table 3.3 percentage volumes involved in recirculating flow are reported. Volume of AVG model has been discretized in five sections, that is, Graft, PA, DA, PV and DV, in order to identify the segment of model most involved in recirculation flow. All of models have a large recirculation area at arterial and venous anastomoses. The segments with the higher recirculation flow volume are

distal artery and distal vein. As 95% of blood flow at arterial anastomosis is sent to the graft, a negative pressure is originated at distal artery section, which draws back distal flow rate. This phenomenon also occurs at distal vein, because of the greater flow rate sent to proximal vein.

Although AVG HFD-3 has the largest total recirculating flow volume, it is worth noting that it presents the smaller percentage of recirculating volume at proximal vein. Moreover, HFD-3 model has the highest percentage of recirculating flow volume in DV. It means that less blood is sent to distal vein. Therefore, it promotes the most flow rate to the heart.

Table 3.3: Percentage of volume involved in recirculating flow.

AVG Models	Vol_rec [%]					
	Graft	PA	DA	PV	DV	Total
Base	0.4067	0.3803	1.5163	0.5341	0.7124	3.5498
Helical	0.8189	0.6545	1.3126	0.6714	0.6820	4.1394
LFD-1	0.2864	0.3483	1.4339	0.4425	0.6859	3.1969
HFD-1	0.2855	0.4276	1.3633	0.4566	0.3113	2.8444
LFD-2	0.3208	0.4480	1.3010	0.5783	0.7501	3.3981
HFD-2	0.3172	0.4705	1.2750	0.5598	0.6132	3.2357
LFD-3	0.3720	0.4210	1.3976	0.5404	0.8041	3.5352
HFD-3	0.5243	0.4145	1.4242	0.1671	1.9728	4.5029

In Figure 3.26, it is possible to see localization of recirculating volumes within models. No zones of recirculation are present inside linear flow divider sections. Recirculating volumes are visualized at the exit of flow divider, due to the transition to a smaller diameter section to one with a larger diameter. A small volume of recirculation is extended for the all length of proximal vein.

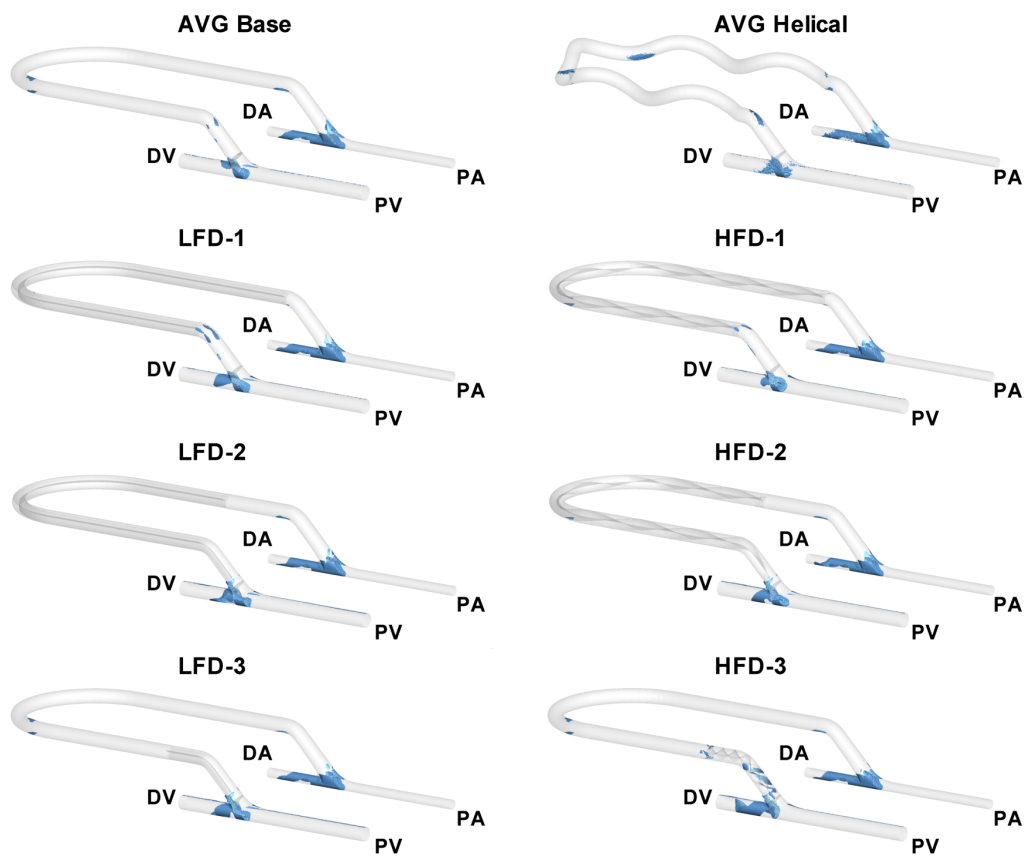


Figure 3.26: Localization of recirculating flow volume in all simulated models.

Chapter 4

Conclusions

The present master thesis work was born with the aim of exploring hemodynamics which takes place within novel designs of arterio-venous grafts, in order to identify the AVG graft which has a minor attitude to promote the insurgence of intimal thickening at venous anastomosis. Venous anastomosis is affected by intimal hyperplasia, because of altered local hemodynamics and injuries that promote growth factors. For that purpose, novel AVG designs were created introducing a flow divider inside them. For these, flow divider positioning and its configuration (LFD or HFD) have been tested. Numerical unsteady-state simulations have been conducted, in order to investigate wall-based and bulkflow hemodynamic conditions at the venous anastomosis, comparing them with hemodynamics of reproduced conventional straight and helical AVGs.

CFD results showed that HFD models induce more favorable hemodynamic conditions with respect to LFD ones. Among HFD AVGs, it is noticed that flow divider position does not particularly influence hemodynamic features, but the considerable factor is the helical pitch used to realize HFD-3 flow divider, that is 4 times smaller than helical pitch of HFD-1 and HFD-2.

As revealed by helicity-based descriptors, bulk flow of HFD-3 is characterized by an helicity amount higher than that of the other models which is comparable, except for the sign, with the reference Helical model. From qualitative helicity descriptor, i.e. LNH, it is possible to see a right-handed helical structure which involves the entire fluid domain at proximal vein. Moreover, HFD-3 exhibits the

lowest recirculation volume in the draining vein.

As regards wall-based descriptors, LFD AVGs exhibit worse performances at region of interest with respect to commercial AVGs, as evidenced by surface area exposed to "disturbed shear" and descriptors mean values. Among HFDs, HFD-3 AVG has a null surface area at venous anastomosis exposed to unfavorable wall shear stress. All of models have low oscillations of WSS and area exposed at high RRT is intrinsically related to TAWSS hemodynamic index.

From percentage differences of mean WSS-based descriptors values with respect to Base model, taken as reference, it is clear that AVG HFD-3 shows better performance than all the other investigated models. It considerably reduce unfavorable hemodynamic features at the venous anastomosis, overcoming the performance of the Helical graft. TAWSS mean value at ROI for HFD-3 graft is, indeed, about 40% higher than the Base model, compared to 5% of Helical model. The same trend is showed by RRT mean, except for the sign. Slight differences has been observed also in terms of SA at ROI exposed to high OSI values between HFD-3 and Base models. Unlike the other models, HFD-3 showed a decrease of OSI mean value at the venous anastomosis.

Promising results observed for HFD-3 configuration make it as a possible solution to overcome common problems of AVGs implanted as vascular access. Showed positive or reduced impact of HFD-3 design on hemodynamics at the site of interest encouraged the idea of a patent. Its design, indeed, allows to overcome also practical problems of helical grafts implantation. In fact, as Van Canneyt et al. [16] sustained, increasing the helix pitch of Helical model, the tension of the skin is greater when AVG is implanted. In HFD-3 model, the internal helix inside straight graft allows to minimize skin tension.

As limitation of this study has to be mentioned the impossibility, at the moment, to compare in silico results with in vivo or in vitro analysis. Moreover, the insurgence of unfavorable thrombogenic processes has to be investigated also in the small channel of arterio-venous graft.

Ringraziamenti

Dopo un anno, trascorso tra alti e bassi affinché questo lavoro prendesse forma, è giunto il tempo dei ringraziamenti.

Desidero ringraziare, in primo luogo, il Professore Umberto Morbiducci, per avermi dato la possibilità di lavorare ad un tema che ha destato il mio entusiasmo fin da subito e per aver tenuto le fila di questo lavoro in maniera impeccabile.

Ringrazio anche l'Ing. Diego Gallo, per il supporto prestatomi come correlatore della tesi.

Infinitamente grazie all'Ing. Giuseppe De Nisco, il miglior tutor che potessi mai desiderare, che passo dopo passo mi ha accompagnato in questo lavoro, mostrandosi paziente e disponibile a chiarire ogni mio dubbio, senza mai farmi mancare il sostegno e l'incoraggiamento. Farò tesoro dei suoi preziosi insegnamenti.

Grazie all'Ing. Karol Calò, aiuto indispensabile nel condurre le simulazioni numeriche oggetto del presente lavoro.

Grazie ai miei genitori, per i sacrifici fatti affinché nulla potesse mancarmi durante tutti questi anni da studentessa fuorisede. Grazie ad Angela, che mi sopporta da quando sono nata; condividere il percorso universitario ci ha permesso di incoraggiarci a vicenda per tagliare insieme questo traguardo. Grazie ad Antonella e Paola, che anche se in questi anni ho trascurato, sono state sempre nei miei pensieri.

Grazie a Laura, punto di riferimento costante. A Maria Luisa, per avermi supportato a distanza. Grazie ai miei amici liguri: Simone, con cui ho passato i mesi più belli all'interno del Poli, spronandomi inconsciamente a dare sempre il meglio, Martina, per i bei momenti condivisi ed anche quelli più difficili, e Davide, per la tenerezza che lo contraddistingue. Grazie a Debora, che mi ricorda ogni giorno

che nella vita non esiste solo il Poli. Grazie a Roberta, sempre pronta a tendermi la mano quando ne avevo bisogno. Un grazie a tutti i ragazzi conosciuti nell'arco di un anno in aula tesisti e alle ragazze con le quali si è instaurato un rapporto più stretto. A Marta, alle nostre pause caffè e alle risate interminabili, che hanno alleggerito le giornate. Un grazie speciale ai parenti e agli amici di Torino, i quali mi hanno dimostrato il loro affetto durante questi anni.

Bibliography

- [1] Spiral Flow™ Grafts - Vascular Flow Technologies.
- [2] Venaflo® II - Bard PV.
- [3] Arthur C. Guyton and John E. Hall. *Textbook of Medical Physiology*. 2006.
- [4] Ilse Van Tricht, Dirk De Wachter, Jan Tordoir, and Pascal Verdonck. Hemodynamics and complications encountered with arteriovenous fistulas and grafts as vascular access for hemodialysis: A review. *Annals of Biomedical Engineering*, 33(9):1142–1157, 2005.
- [5] Jacob A. Akoh. Prosthetic arteriovenous grafts for hemodialysis. *Journal of Vascular Access*, 10(3):137–147, 2009.
- [6] L. Berardinelli. Grafts and Graft Materials as Vascular Substitutes for Haemodialysis Access Construction. *European Journal of Vascular and Endovascular Surgery*, 32(2):203–211, 2006.
- [7] A. S. Bode and J. H M Tordoir. Vascular access for hemodialysis therapy. Technical Report January 2013, 2013.
- [8] M. S. Lemson, J. H.M. Tordoir, M. J.A.P. Daemen, and P. J.E.H.M. Kitslaar. Intimal hyperplasia in vascular grafts. *European Journal of Vascular and Endovascular Surgery*, 19(4):336–350, 2000.
- [9] Hiroaki Haruguchi and Satoshi Teraoka. Intimal hyperplasia and hemodynamic factors in arterial bypass and arteriovenous grafts: A review. *Journal of Artificial Organs*, 6(4):227–235, 2003.

- [10] Xiao Liu, Anqiang Sun, Yubo Fan, and Xiaoyan Deng. Physiological Significance of Helical Flow in the Arterial System and its Potential Clinical Applications. *Annals of Biomedical Engineering*, 43(1):3–15, 2014.
- [11] Umberto Morbiducci, Raffaele Ponzini, Mauro Grigioni, and Alberto Redaelli. Helical flow as fluid dynamic signature for atherogenesis risk in aortocoronary bypass. A numeric study. *Journal of Biomechanics*, 40(3):519–534, 2007.
- [12] Michael Heise, S. Schmidt, U. Krüger, R. Pfitzmann, H. Scholz, P. Neuhaus, and U. Settmacher. Local haemodynamics and shear stress in cuffed and straight PTFE-venous anastomoses: An in-vitro comparison using particle image velocimetry. *European Journal of Vascular and Endovascular Surgery*, 26(4):367–373, 2003.
- [13] Michael Heise, Inga Husmann, Ann Kathrin Grneberg, Alexander Knobel, Petra Kirschner, and Christoph Heidenhain. Comparison of straight and Venaflo-type cuffed arteriovenous ePTFE grafts in an animal study. *Journal of Vascular Surgery*, 53(6):1661–1667, 2011.
- [14] F. Ghalichi E. Samiei M. Sarmast, H. Niroomand-Oscuii. Evaluation of the hemodynamics in straight 6-mm and tapered 6- to 8-mm grafts as upper arm hemodialysis vascular access. pages 797–811, 2014.
- [15] Colin G Caro, Nick J Cheshire, and Nick Watkins. Preliminary comparative study of small amplitude helical and conventional ePTFE arteriovenous shunts in pigs. *Journal of the Royal Society, Interface / the Royal Society*, 2(3):261–6, 2005.
- [16] K. Van Canneyt, U. Morbiducci, S. Eloot, G. De Santis, P. Segers, and P. Verdonck. A computational exploration of helical arterio-venous graft designs. *Journal of Biomechanics*, 46(2):345–353, 2013.
- [17] Foad Kabinejadian, Michael McElroy, Andres Ruiz-Soler, Hwa Liang Leo, Mark A. Slevin, Lina Badimon, and Amir Keshmiri. Numerical assessment

- of novel helical/spiral grafts with improved hemodynamics for distal graft anastomoses. *PLoS ONE*, 11(11), 2016.
- [18] Foad Kabinejadian, Boyang Su, Dhanjoo N. Ghista, Munirah Ismail, Sangho Kim, and Hwa Liang Leo. Sequential venous anastomosis design to enhance patency of arterio-venous grafts for hemodialysis. *Computer Methods in Biomechanics and Biomedical Engineering*, 20(1):85–93, 2017.
- [19] Connor V. Cunnane, Eoghan M. Cunnane, and Michael T. Walsh. A Review of the Hemodynamic Factors Believed to Contribute to Vascular Access Dysfunction. *Cardiovascular Engineering and Technology*, 8(3):280–294, 2017.
- [20] James F. Price. Lagrangian and Eulerian Representations of Fluid Flow: Kinematics and the Equation of Motion. page 91, 2006.
- [21] Rui Lima, Yohsuke Imai, Takuji Ishikawa, and Monica Oliveira. *Visualization and Simulation of Complex Flows in Biomedical Engineering*, volume 12. 2014.
- [22] Diego Gallo, David A. Steinman, Payam B. Bijari, and Umberto Morbiducci. Helical flow in carotid bifurcation as surrogate marker of exposure to disturbed shear. *Journal of Biomechanics*, 45(14):2398–2404, 2012.
- [23] Diego Gallo, David A. Steinman, and Umberto Morbiducci. Insights into the co-localization of magnitude-based versus direction-based indicators of disturbed shear at the carotid bifurcation. *Journal of Biomechanics*, 49(12):2413–2419, 2016.
- [24] Umberto Morbiducci, Diego Gallo, Raffaele Ponzini, Diana Massai, Luca Antiga, Franco M. Montevecchi, and Alberto Redaelli. Quantitative analysis of bulk flow in image-based hemodynamic models of the carotid bifurcation: The influence of outflow conditions as test case. *Annals of Biomedical Engineering*, 38(12):3688–3705, 2010.
- [25] Demosthenes Katritsis, Lambros Kaiktsis, Andreas Chaniotis, John Pantos, Efstathios P. Efstathopoulos, and Vasilios Marmarelis. Wall Shear Stress:

- Theoretical Considerations and Methods of Measurement. *Progress in Cardiovascular Diseases*, 49(5):307–329, 2007.
- [26] Amit K. Mitra, Deepak M. Gangahar, and Devendra K. Agrawal. Cellular, molecular and immunological mechanisms in the pathophysiology of vein graft intimal hyperplasia. *Immunology and Cell Biology*, 84(2):115–124, 2006.
- [27] Themistoklis A. Manos, Dimitrios P. Sokolis, Athina T. Giagini, Constantinos H. Davos, John D. Kakisis, Eleftherios P. Kritharis, Nikos Stergiopoulos, Panayotis E. Karayannacos, and Sokrates Tsangaris. Local hemodynamics and intimal hyperplasia at the venous side of a porcine arteriovenous shunt. *IEEE Transactions on Information Technology in Biomedicine*, 14(3):681–690, 2010.
- [28] Jan Tordoir Pascal Verdonck Ilse Van Tricht, Dirk De Wachter. Comparison of the hemodynamics in 6 mm and 4 – 7 mm hemodialysis grafts by means of CFD. 39:226–236, 2006.

Appendix A

A.1 Selection of ROI

```
1 close all
2 clear all
3 clc
4
5 imp=importdata(' ./Descrittori_emodinamici_AVG_LFD3.tec ');
6 k1=strfind(imp.textdata{2}, 'N=');
7 k2=strfind(imp.textdata{2}, ', ');
8 N=str2num(imp.textdata{2}(k1+2:k2(1)-1));
9 coord=imp.data(1:N,1:3);
10 mconn=imp.data(N+1:end,1:3);
11 descr=imp.data(1:N,4:6);
12
13 % Coordinates of models
14 c=find(coord(:,1) <=0.007 & coord(:,2) <=0.0095 & coord(:,2)
        >=(0.003+min(coord(:,2))) & coord(:,3) >=0.13 & coord
       (:,3) <=0.148 );
15
16 % Coordinates of helical model
17 c=find(coord(:,1) <=0.010 & coord(:,2) <=0.0095 & coord(:,2)
        >=(0.003+min(coord(:,2))) & coord(:,3) >=0.1325 & coord
       (:,3) <=0.1505 );
```

```
18
19 plot3(coord(c,3),coord(c,2),coord(c,1),'.')
20
21 descr_new=0*descr;
22 descr_new(:,1)=10+descr_new(:,1);
23 descr_new(c,:)=descr(c,:);
24 DATA=[coord descr_new];
25
26 fid=fopen('./Descrittori_emodinamici_AVG_LFD3_ROI.dat','wt
    ');
27 fprintf(fid,'VARIABLES = X,Y,Z,TAWSS_graftLFD3_ROI,
    OSI_graftLFD3_ROI,RRT_graftLFD3_ROI \n' );
28 fprintf(fid,'ZONE N=296648,E=592976,F=FEPOINT,ET=TRIANGLE
    \n' );
29 fprintf(fid,'%e %e %e %e %e %e\n',DATA);
30 fprintf(fid,'%i %i %i\n',mconn);
31 fclose(fid);
```

Appendix B

B.1 Axial velocity

```
1 clear all
2 close all
3 clc
4
5 %% DIVISIONE A SECONDA DEL BRANCHING
6
7 %% IMPORTAZIONE DATI
8 distance=importdata('./AVG_helical_MEAN-VELdata-GroupIds.
    tec'); % change! VARIABLES = X,Y,Z, ClippingArray ,Vx,Vy,
    Vz, GroupIds
9 k1=strfind(distance.textdata{2}, 'N=');
10 k2=strfind(distance.textdata{2}, ', ');
11 N=str2num(distance.textdata{2}(k1+2:k2(1)-1));
12 distance.data(N+1:end,:) = [];
13 plot3(distance.data(:,1), distance.data(:,2), distance.data
   (:,3), '.');
14
15 VELA=zeros(length(distance.data),1);
16 meta=mean(distance.data(:,1));
17
18 for i=1:N
```

```
19     if distance.data(i,1)<meta
20
21         if (distance.data(i,2)>0.006 && distance.data(i,2)
22             <0.019)
23             VELa(i)=-distance.data(i,6);
24
25         elseif distance.data(i,3)<0.025
26             VELa(i)=-distance.data(i,5);
27
28         else
29             VELa(i)=distance.data(i,7);
30         end
31     else
32         if (distance.data(i,2)>0.006 && distance.data(i,2)
33             <0.019)
34             VELa(i)=distance.data(i,6);
35
36         elseif distance.data(i,3)<0.025
37             VELa(i)=-distance.data(i,5);
38
39         else
40             VELa(i)=-distance.data(i,7);
41         end
42     end
43
44     eval(['save VELa_Helical VELa']);
```

B.2 Recirculating flow volume

```
1 clear all
2 close all
3 clc
4
5 % calcolo Volume a centro cella
6 imp=importdata( './Cell_Volume_AVG_Helical-GroupIds.
7         tec ');
8 k1=strfind(imp.textdata{2}, 'N=');
9 k2=strfind(imp.textdata{2}, ',');
10 N=str2num(imp.textdata{2}(k1+2:k2(1)-1));
11 coord=imp.data(1:N,1:3);
12 mconn=imp.data(N+1:end,1:4);
13
14 V=imp.data(1:N,5);
15 % importazione file .mat contenente velocita assiale
16 load VELA_Helical.mat
17
18 ind_neg=find(VELa<0);
19 AbsVolRec=sum(abs(V(ind_neg)));
20 PercVolRec=sum(abs(V(ind_neg)))*100/sum(abs(V));
21 rec=imp.data(ind_neg,5:6);
22
23 %Legend GroupIds
24 %Graft=3, PA=0, DA=2, PV=6, DV=5 (Models Base ,LFD1,
25         HFD1)
26 %Graft=2, PA=0, DA=6, PV=5, DV=4 (Models Helical ,
27         LFD2,HFD2,LFD3,HFD3)
28
29 ind_G=find(rec(:,2)==2);
30 Vol_Rec_G=sum(abs(rec(ind_G,1)));
31 PercVolRec_G=sum(abs(rec(ind_G,1)))*100/sum(abs(V))
```

```
30     ind_PA=find ( rec (: ,2) ==0);
31     Vol_Rec_PA=sum ( abs ( rec ( ind_PA ,1) ) );
32     PercVolRec_PA=sum ( abs ( rec ( ind_PA ,1) ) ) *100/sum ( abs ( V) )
33
34     ind_DA=find ( rec (: ,2) ==6);
35     Vol_Rec_DA=sum ( abs ( rec ( ind_DA ,1) ) );
36     PercVolRec_DA=sum ( abs ( rec ( ind_DA ,1) ) ) *100/sum ( abs ( V) )
37
38     ind_PV=find ( rec (: ,2) ==5);
39     Vol_Rec_PV=sum ( abs ( rec ( ind_PV ,1) ) );
40     PercVolRec_PV=sum ( abs ( rec ( ind_PV ,1) ) ) *100/sum ( abs ( V) )
41
42     ind_p=find ( VELa>0); %verso z opposto
43     recp=imp . data ( ind_p , 5:6 );
44     ind_DV=find ( recp (: ,2) ==4);
45     Vol_Rec_DV=sum ( abs ( recp ( ind_DV ,1) ) );
46     PercVolRec_DV=sum ( abs ( recp ( ind_DV ,1) ) ) *100/sum ( abs ( V) )
47
48     PercS=PercVolRec_G+PercVolRec_PA+PercVolRec_DA+
49           PercVolRec_PV+PercVolRec_DV
50
51     S=Vol_Rec_G+Vol_Rec_PA+Vol_Rec_DA+Vol_Rec_PV+
52       Vol_Rec_DV
53
54     ind=ones (N,1);
55     for i=1:length ( ind_neg )
56         if imp . data ( ind_neg ( i) ,6) ==0 | imp . data ( ind_neg ( i)
57             ,6) ==2 | imp . data ( ind_neg ( i) ,6) ==5 | imp . data (
58                 ind_neg ( i) ,6) ==6
59             ind ( ind_neg ( i) ,1) =-1;
60         end
61     end
62     for i=1:length ( ind_p )
```

```
58         if imp.data(ind_p(i),6)==4
59             ind(ind_p(i),1)=-1;
60         end
61     end
62
63 DATA=[imp.data(1:N,1:3) abs(V) ind imp.data(1:N,6)];
64
65 fid=fopen('/Volumes/Katia/TESI/Vol_rec/Vol_recHelical.tec',
66           'wt');
67 fprintf(fid, 'VARIABLES = X,Y,Z,Volume,Ind,GroupIds \n' );
68 fprintf(fid, 'ZONE N=1288970,E=7303670,F=FEPOINT,ET=
69           TETRAHEDRON \n' );
70 fprintf(fid, '%e %e %e %e %e %e \n',DATA);
71 fprintf(fid, '%i %i %i %i \n',mconn);
72 fclose(fid);
```